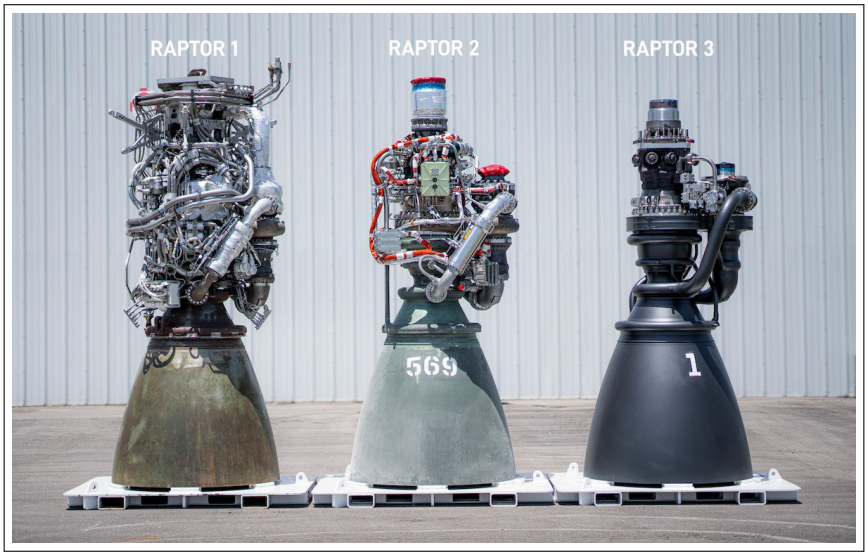
Advanced Computational Fluid Dynamics Research

Advanced CFD Simulation of Internal Flow Dynamics in the Raptor 2 Combustion Chamber and Nozzle



Prepared by

YAZIDI Hamza

25 July 2025

Abstract

This report presents a comprehensive Computational Fluid Dynamics (CFD) study of the internal flow dynamics within the combustion chamber and nozzle of SpaceX's Raptor 2 engine, a cutting-edge Full-Flow Staged Combustion (FFSC) engine fueled by methane (CH_4) and oxygen (O_2). The objective of this research is to characterize the complex flow behavior, combustion efficiency, and performance parameters under both sea-level and vacuum conditions, providing critical insights into next-generation propulsion system optimization.

The methodology combines multiple modeling tools in a structured workflow: preliminary thermodynamic analysis via NASA's Chemical Equilibrium with Applications (CEA), geometric refinement using Rocket Propulsion Analysis (RPA), and preburner combustion modeling with Cantera in Python. A 2D axisymmetric CFD model was developed, integrating high-resolution meshing, realistic boundary conditions, and turbulence-chemistry interaction based on the GRI-Mech 3.0 chemical mechanism.

The simulation achieved a peak chamber pressure of 296 bar, a 1.33 % deviation from the nominal 300 bar of the real Raptor 2 engine, and combustion temperatures up to 3720 K. Exhaust gases accelerated to 3420 $\mathrm{m\,s^{-1}}$ with a Mach number of 3.93, validating the model's fidelity. Species mass fraction profiles demonstrated near-complete combustion, with CH_4 and O_2 residuals below 10^{-10}, and revealed localized zones of incomplete reactions near wall regions. Minor numerical artifacts in the Mach number field, due to wall boundary effects, were identified and corrected in post-processing.

Comparison with actual Raptor 2 performance data revealed high agreement across key parameters including thrust, specific impulse, and exit velocity, with deviations generally below 3 %. These findings highlight the accuracy and reliability of the proposed CFD workflow and underscore its value as a predictive design tool for advanced rocket engines.

This project not only validates current design methods but also establishes a solid foundation for future enhancements, such as regenerative cooling modeling and injector flow refinement. More broadly, it demonstrates the potential of student-led, high-fidelity CFD modeling in contributing meaningfully to aerospace propulsion research. By closely reproducing the behavior of the Raptor 2 engine, this work supports ongoing efforts in the industry toward reusable, efficient, and high-performance engines a key enabler of missions like SpaceX's Mars colonization initiative.

Contents

Contents ii

List of Figures iv

List of Tables vi

Nomenclature viii

I Introduction 1
- I.1 Context and Motivation . . . 1
- I.2 Overview of the Raptor 2 Engine . . . 1
- I.3 Full-Flow Staged Combustion (FFSC) . . . 3

II Methodology 6
- II.1 Geometry . . . 6
  - II.1.1 Preliminary Design Using NASA CEA . . . 6
  - II.1.2 Design Using Rocket Propulsion Analysis (RPA) . . . 8
  - II.1.3 Comparison Between NASA CEA and RPA . . . 12
  - II.1.4 Geometry Visualization . . . 15
  - II.1.5 Sizing the Injectors . . . 17
- II.2 Meshing . . . 22
- II.3 Boundary conditions . . . 24
- II.4 Governing equations . . . 25
- II.5 Modeling of Combustion . . . 27
- II.6 Chemical kinetics and Thermochemistry properties . . . 28
- II.7 Solver settings . . . 29

III Results 30
- III.1 Convergence analysis . . . 30
- III.2 Pressure . . . 32
- III.3 Temperature . . . 33
- III.4 Velocity . . . 34
- III.5 Mach Number . . . 35
- III.6 Species Mass Fraction . . . 36
  - III.6.1 Reactants Mass Fraction . . . 36
  - III.6.2 Products Mass Fraction . . . 37
  - III.6.3 Other Species Mass Fraction . . . 38

III.7 Results of the 8 Simulations 39

IV Discussion **40**

IV.1 Comparison Between Ansys Results and RPA results 40

IV.2 Why FFSC ? 41

IV.3 The Reasons Behind O/F=3.6 43

IV.4 Comparison Between Vacuum and Sea Level 46

IV.5 Comparison Between our Results and Real Raptor 2 engine 48

V Conclusion **49**

References **51**

List of Figures

1 SpaceX Raptor 2 Engine . . . 2
2 Full Flow Staged Combustion (FFSC) . . . 4
3 Schematic of Typical Propellant Flow . . . 5
4 RPA Logo . . . 9
5 Mach Number Distribution in RPA . . . 11
6 Pressure Distribution in RPA . . . 11
7 Temperature Distribustion in RPA . . . 12
8 Raptor 2 Sketch . . . 16
9 Raptor 2 3D Inner Wall . . . 16
10 Coaxial Injector Gemetry . . . 17
11 Discharge coefficient . . . 18
12 Injector Geometry . . . 20
13 Mesh Near the Wall . . . 22
14 Mesh in the Combustion Chamber . . . 23
15 Mesh in the Throat . . . 23
16 Residuals in Function of Iterations . . . 30
17 Mass Flow Rate in Function of Iterations . . . 30
18 Pressure at the Outlet in Function of Iterations . . . 31
19 Temperature at the Outlet in Function of Iterations . . . 31
20 Velocity at the Outlet in Function of Iterations . . . 31
21 Mach Number at the Outlet in Function of Iterations . . . 31
22 Pressure Distribution . . . 32
23 Pressure in the wall in and in the axis . . . 32
24 Temperature Distribution . . . 33
25 Temperature in the wall in and in the axis . . . 33
26 Temperature Distribution zoom in the Combustion Chamber . . . 33
27 Velocity Distribution . . . 34
28 Velocity in the wall in and in the axis . . . 34
29 Velocity Distribution zoom near the wall . . . 34
30 Mach Number Distribution . . . 35
31 Mach Number in the wall in and in the axis . . . 35
32 Corrected Mach Number Distribution . . . 36
33 Corrected Mach Number in the wall in and in the axis . . . 36
34 Corrected Mach Number Distribution zoom near the wall . . . 36
35 O_2 Mass fraction . . . 36
36 CH_4 Mass fraction . . . 36
37 O_2 Mass fraction zoom in the Combustion Chamber . . . 37

38 CH_4 Mass fraction zoom in the Combustion Chamber 37
39 H_2O Mass fraction 37
40 CO_2 Mass fraction 37
41 CO Mass fraction 38
42 Other Radicals Species Mass fraction 38
43 Other Fuel Molecules Mass fraction 38
44 Other Oxidizer Molecules Mass fraction 39
45 Program interface 44

List of Tables

1 SpaceX Raptor 2 characteristics in sea level . . . 3
2 Composition of combustion products at preburner outlets from Cantera (mass fractions) . . . 5
3 Input parameters for design . . . 6
4 Calculated parameters . . . 8
5 RPA configuration parameters . . . 9
6 Combustion properties . . . 9
7 Engine performance . . . 10
8 Chamber size parameters . . . 10
9 Nozzle size parameters . . . 10
10 Mass flow and mixture ratio . . . 10
11 Combustion products composition . . . 11
12 Comparison of performance parameters between RPA and NASA CEA results 13
13 Comparison of thermodynamic properties between RPA and NASA CEA results . . . 13
14 Comparison of geometric parameters between RPA and NASA CEA results 13
15 Comparison of combustion product mass fractions between RPA and NASA CEA results . . . 14
16 Thrust chamber injectors pressure losses . . . 18
17 Density of Propellant Before Injection . . . 19
18 Injection Areas for Oxidizer and Fuel . . . 20
19 Injector Diameters: Maximum vs Chosen . . . 20
20 Final Propellants Areas . . . 20
21 Injector flow parameters . . . 21
22 Injector length parameters . . . 21
23 Mesh divisions configuration . . . 22
24 Simulation boundary conditions . . . 25
25 Under-Relaxation Factors . . . 30
26 Initial Values . . . 30
27 Chemical species groups . . . 39
28 Performance Results . . . 39
29 Comparison between ANSYS and RPA Results . . . 40
30 Simulation Results Comparison WHY FFSC . . . 41
31 Performance Comparison by O/F Ratio . . . 43
32 Results of O/F Cantera Simulation . . . 45
33 Composition of combustion products at preburner outlets from Cantera O/F=3 (mass fractions) . . . 45

34 Performance Comparison: Vacuum vs Sea Level 46
35 Comparison between Raptor 2 and Our Simulation 48

Nomenclature

Symbols

A	Area [m^2]
A_c	Chamber cross-sectional area [m^2]
A_e	Nozzle exit area [m^2]
A_t	Throat area [m^2]
c^*	Characteristic velocity [$\mathrm{m\,s}^{-1}$]
c_e	Effective exhaust velocity [$\mathrm{m\,s}^{-1}$]
C_d	Discharge coefficient [–]
C_f	Thrust coefficient [–]
D_c	Chamber diameter [m]
D_e	Nozzle exit diameter [m]
D_t	Throat diameter [m]
F	Thrust [N]
g_0	Standard gravity [$\mathrm{m\,s}^{-2}$]
I_{sp}	Specific impulse [s]
L_c	Chamber length [m]
L^*	Characteristic chamber length [m]
M	Mach number [–]
$\dot{m}$	Mass flow rate [$\mathrm{kg\,s}^{-1}$]
P	Pressure [Pa]
R	Gas constant [J/(kgK)]
T	Temperature [K]
v	Velocity [$\mathrm{m\,s}^{-1}$]
V_c	Chamber volume [m^3]
γ	Specific heat ratio [–]
ρ	Density [$\mathrm{kg\,m}^{-3}$]
ΔP	Pressure drop [Pa]
α	Oxidizer excess coefficient [–]
∇	Gradient operator
∂	Partial derivative
μ	Dynamic viscosity [Pa s]
μ_t	Turbulent viscosity [Pa s]
k_t	Turbulent thermal conductivity [W/(mK)]
C_p	Specific heat at constant pressure [J/(kgK)]
k_f	Forward reaction rate coefficient

A	Pre-exponential factor
E_a	Activation energy [$\mathrm{J\,mol^{-1}}$]
n	Temperature exponent
$\tilde{R}_j$	Net reaction rate of species j

Subscripts

c	Chamber condition
e	Exit condition
f	Fuel
o	Oxidizer
t	Throat condition

Abbreviations

CFD	Computational Fluid Dynamics
CEA	Chemical Equilibrium with Applications
FFSC	Full-Flow Staged Combustion
GCH_4	Gaseous Methane
GO_2	Gaseous Oxygen
LOX	Liquid Oxygen
O/F	Oxidizer-to-Fuel ratio
RPA	Rocket Propulsion Analysis
RANS	Reynolds-Averaged Navier-Stokes
PDF	Probability Density Function
SIMPLE	Semi-Implicit Method for Pressure-Linked Equations
k-ω SST	Shear Stress Transport turbulence model
Sc_t	Turbulent Schmidt number
Le	Lewis number

Chemical Species

CH_4	Methane
CO	Carbon monoxide
CO_2	Carbon dioxide
H_2	Hydrogen
H_2O	Water
O_2	Oxygen
OH	Hydroxyl radical
H	Atomic hydrogen
O	Atomic oxygen
HO_2	Hydroperoxyl radical

CH_3	Methyl radical
HCO	Formyl radical
CH_2CO	Ketene
CH_3OH	Methanol
C_2H_2	Acetylene
C_2H_4	Ethylene
C_2H_6	Ethane
C_3H_8	Propane
H_2O_2	Hydrogen peroxide
CH_2O	Formaldehyde

I Introduction

I.1 Context and Motivation

Rocket propulsion plays a critical role in space exploration, enabling vehicles to overcome Earth's gravity and travel into orbit and beyond. At the heart of these propulsion systems lies the combustion chamber and nozzle, where high-pressure, high-temperature gases are generated and accelerated to produce thrust. Understanding the complex fluid dynamics within these components is essential for optimizing performance and ensuring structural integrity.

Computational Fluid Dynamics (CFD) has become an indispensable tool in modern propulsion system design, allowing engineers to simulate and analyze internal flows with high precision, significantly reducing the need for costly and time-consuming physical testing.

In this context, SpaceX's Raptor 2 engine stands as a state-of-the-art example of a full-flow staged combustion engine powered by liquid methane and liquid oxygen (methalox), offering high performance and reusability.

This study focuses on the internal flow behavior within the combustion chamber and converging-diverging nozzle of the Raptor 2. To maintain a manageable scope and focus on core flow characteristics, the injector system has been excluded from the simulation. This simplification allows for a detailed analysis of velocity, pressure, and thermal profiles that are critical to engine performance.

I.2 Overview of the Raptor 2 Engine

The Raptor 2 engine, developed by SpaceX, represents a major leap in rocket propulsion technology. It is a full-flow staged combustion engine (FFSC) that uses methane (CH_4) and liquid oxygen (LOX) as propellants, making it suitable for long-term missions, including potential Mars colonization. Designed for high efficiency and reusability, Raptor 2 delivers significantly more thrust and is mechanically simpler compared to its predecessor.

Its advanced architecture, which includes separate fuel and oxidizer preburners, enables improved combustion stability and thermal management. This section outlines the key performance parameters and design features that make Raptor 2 a benchmark in modern rocket engine development.

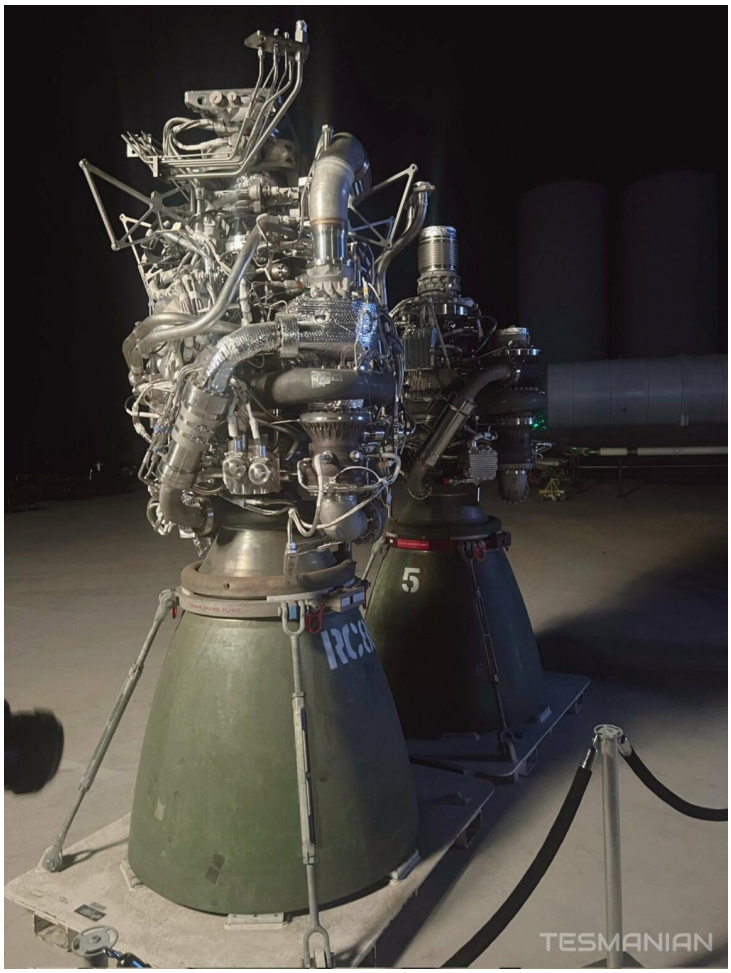


Figure 1: *SpaceX Raptor 2 Engine*

The values presented in the Table 1 may vary slightly from one source to another due to differences in estimation methods, test conditions, or data disclosure policies. One notable discrepancy concerns the total propellant mass flow rate: while many sources cite a total mass flow of approximately 650 kg/s for the Raptor 2 engine, a calculation based on the well-known thrust-specific impulse relationship:

$$I_{sp} = \frac{T}{\dot{m} \cdot g_0} \tag{1}$$

Substituting the given thrust (2.3 MN) and specific impulse (327 s), the calculated total mass flow rate is around 718 kg/s. For consistency and accuracy in comparison with our simulation results, this calculated value will be adopted throughout the report.

Table 1: *SpaceX Raptor 2 characteristics in sea level*

Parameter	Value
Dimensions	
Nozzle exit diameter	1.3 m
Throat to exit length	1.5 m
Area Ratio	34.34
Propellant	
Fuel	GCH_4
Oxidizer	GO_2
O/F ratio	3.6
GCH_4 inlet temperature	808 K
GO_2 inlet temperature	707 K
Fuel mass flow	155 kg/s
Oxidizer mass flow	563 kg/s
Performances	
I_{SP} (Sea Level)	327 s
Thrust (Sea Level)	2.3 MN
Chamber pressure (nominal)	300 bar
Design Features	
Cooling technique	Regenerative cooling
Injector design	Coaxial swirl injectors

I.3 Full-Flow Staged Combustion (FFSC)

Full-flow staged combustion (FFSC) is a type of staged combustion cycle with a dual-shaft design that uses both oxidizer-rich and fuel-rich preburners, where the entire supply of both propellants passes through the turbines. The fuel turbopump is driven by the fuel-rich preburner, and the oxidizer turbopump is driven by the oxidizer-rich preburner.

The advantages of the full-flow staged combustion cycle include turbines operating at lower temperatures and pressures due to the increased mass flow, which results in longer engine lifespans and higher reliability. For example, up to 25 flights were anticipated for an engine design studied by the German Aerospace Center (DLR) as part of the SpaceLiner project, while up to 1000 flights are expected for SpaceX's Raptor engine. Additionally, the full-flow cycle eliminates the need for an inter-propellant turbine seal, which is typically required to separate oxidizer-rich gases from the fuel turbopump or fuel-rich gases from the oxidizer turbopump, thereby enhancing overall reliability. Since the use of both fuel-rich and oxidizer-rich preburners leads to complete gasification of each propellant before entering the combustion chamber, FFSC engines belong to a broader category of rocket engines known as gas-gas engines.

The complete gasification of the components allows for faster chemical reactions in the combustion chamber, enabling a smaller combustion chamber. This, in turn, makes it possible to increase the chamber pressure, which improves efficiency. The potential drawbacks of the full-flow staged combustion (FFSC) cycle include stricter material requirements, increased engineering complexity, and a greater number of components due to the presence of two preburners, compared to a single-shaft staged combustion cycle.

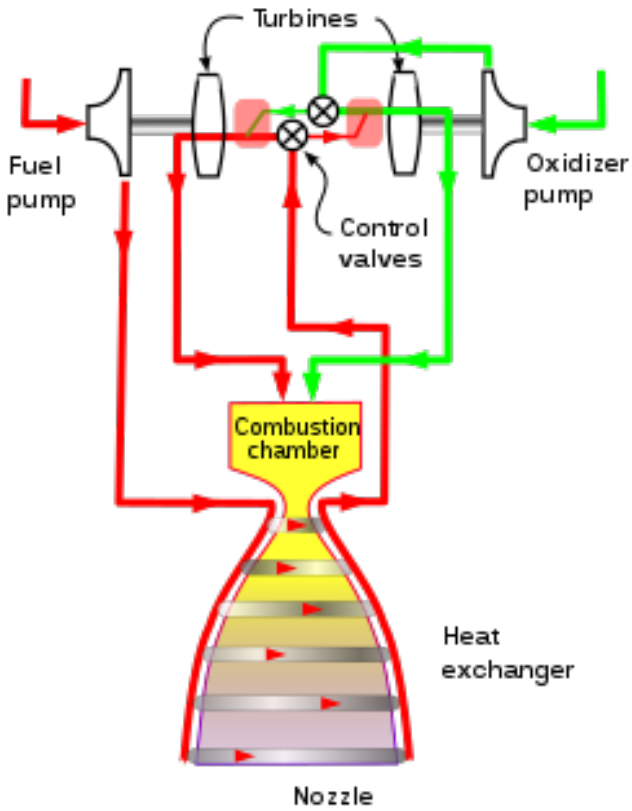


Figure 2: *Full Flow Staged Combustion (FFSC)*

As of 2024, four FFSC rocket engines have been tested on the ground: the Soviet RD-270 project using storable propellants developed by Energomash in the 1960s, the Integrated Powerhead Demonstrator hydrolox engine funded by the U.S. government and developed by Aerojet Rocketdyne in the mid-2000s,

the methalox Raptor engine by SpaceX capable of flight and first tested in February 2019, and the methalox engine developed for the first stage of Stoke Space's Nova vehicle in 2024.

The first flight test of a full-flow staged combustion engine occurred on July 25, 2019, when SpaceX flew their Raptor FFSC methalox engine on the Starhopper test vehicle at their launch site in South Texas. As of January 2025, the Raptor remains the only FFSC engine to have flown on a launch vehicle.

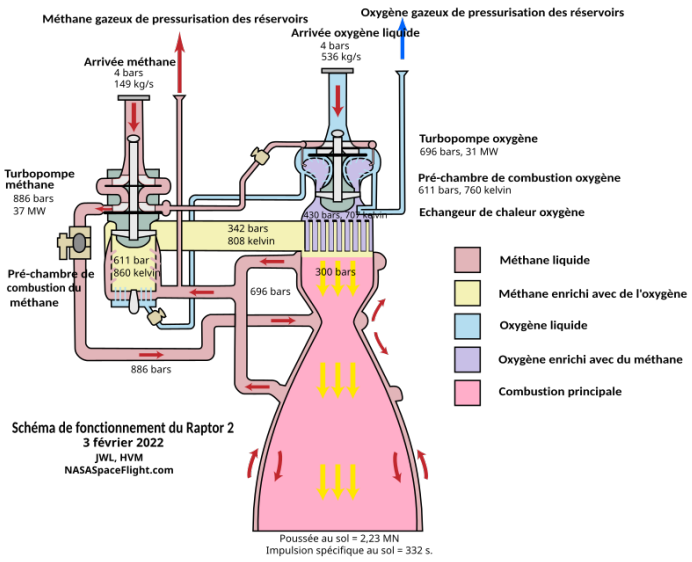


Figure 3: *Schematic of Typical Propellant Flow*

Table 2: *Composition of combustion products at preburner outlets from Cantera (mass fractions)*

Species	Fuel (CH_4 preburner outlet)	Oxidizer (LOX preburner outlet)
CH_4 (Methane)	0.82	0
O_2 (Oxygen)	0	0.94
CO_2 (Carbon dioxide)	0.1	0.032
H_2O (Water vapor)	0.071	0.026
CO (Carbon monoxide)	0.0035	0
H_2 (Hydrogen)	0.0017	0
C_2H_6 (Ethane)	0.0019	0

II Methodology

II.1 Geometry

II.1.1 Preliminary Design Using NASA CEA

In order to initiate the preliminary design of our rocket engine, we will use NASA CEA (Chemical Equilibrium with Applications) to obtain key thermodynamic and performance parameters such as specific impulse, characteristic velocity, combustion temperature, and exhaust gas properties. These parameters are essential for defining the initial geometry of the combustion chamber and nozzle, including the throat area, expansion ratio, chamber length, and diameters. The data obtained from NASA CEA will serve as a foundation for applying ideal rocket theory equations and empirical correlations to estimate the main dimensions and guide the early design stages.

Table 3: *Input parameters for design*

Parameter	Value	Unit	Source / Note
Thrust Coefficient (C_f)	1.8416	—	From NASA CEA
Specific Impulse by Mass (I_{sp})	3546.5	m/s	From NASA CEA
Characteristic Velocity (c*)	1925.8	m/s	From NASA CEA
Throat Sonic Velocity (v_{st})	1261.5	m/s	From NASA CEA
Exit Mach Number (M_e)	3.731	—	From NASA CEA
Chamber Temperature (T_c)	3950.36	K	From NASA CEA
Throat Pressure (P_t)	173.33	bar	From NASA CEA
Throat Temperature (T_t)	3749.45	K	From NASA CEA
Throat Specific Heat Ratio (γ_t)	1.1338	—	From NASA CEA
Molecular Weight (M)	22.210	g/mol	From NASA CEA
Gas Constant (R)	374.36	J/(kg·K)	R_u = 8314.46 / M
Throat Density (ρ_t)	12.349	kg/m^3	From NASA CEA
L* (Characteristic Chamber Length)	0.9	m	Chosen parameter
L_c (Chamber Length)	0.5	m	Chosen parameter

The throat area A_t and throat diameter D_t of the nozzle were calculated based on the definition of characteristic velocity : $c^* = \frac{P_c \cdot A_t}{\dot{m}}$. Solving for A_t and substituting the given values yielded $A_t \approx 0.04613\,\mathrm{m}^2$.

$$D_t = \sqrt{\frac{4A_t}{\pi}} \approx 0.2424 \text{ m} \quad (242.4 \text{ mm}) \tag{2}$$

Using a characteristic length $L^* = \frac{V_c}{A_t}$, the chamber volume was obtained as :

$$V_c = L^* \cdot A_t = 0.04152 \text{ m}^3 \quad (3)$$

Considering a cylindrical geometry with a chamber length of 0.5 m, the chamber diameter was calculated :

$$D_c = \sqrt{\frac{4V_c}{\pi L_c}} \approx 0.325 \text{ m} \quad (325 \text{ mm}) \quad (4)$$

The chamber area was then determined as $A_c \approx 0.083\,\text{m}^2$. For the nozzle exit, with an area ratio $A_e/A_t = 34.34$, the exit area was calculated as $A_e \approx 1.584\,\text{m}^2$.

$$D_e = \sqrt{\frac{4A_e}{\pi}} \approx 1.42 \text{ m} \quad (1420 \text{ mm}) \quad (5)$$

To validate the flow conditions and thrust performance of the designed engine, a series of calculations were carried out based on NASA CEA output data. The mass flow rate at the throat was verified using the continuity equation:

$$\dot{m} = \rho_t \cdot A_t \cdot v_t \quad (6)$$

Solving for the throat velocity:

$$v_t = \frac{\dot{m}}{\rho_t \cdot A_t} \quad (7)$$

Using $\rho_t = 12.349$ kg/m^3, $A_t = 0.0461$ m^2, and $\dot{m} = 718$ kg/s, we obtain $v_t \approx 1261$ m/s, consistent with the sonic velocity reported by CEA. The thrust was computed using two approaches.

First, via specific impulse:

$$F = \dot{m} \cdot I_{sp} \quad (8)$$

With $I_{sp} = 3546.5$ m/s, this yields:

$$F \approx 2.547 \times 10^6 \text{ N} \quad (9)$$

Alternatively, using the thrust coefficient $C_F = 1.8416$, chamber pressure $P_c = 300 \times 10^5$ Pa, and throat area $A_t = 0.0461$ m^2:

$$F = C_F \cdot P_c \cdot A_t \quad (10)$$

$F \approx 2.547 \times 10^6$ N confirming consistency between both methods.

The effective exhaust velocity c_e is approximately equal to the specific impulse by mass:

$$c_e \approx 3546.5 \text{ m/s} \quad (11)$$

From the CEA exit conditions exit pressure $P_e = 1.013$ bar, exit temperature $T_e = 2317$ K, density $\rho_e = 0.1287$ kg/m^3, and Mach number $M_e = 3.728$ the exit velocity can be calculated by:

$$v_e = M_e \cdot \sqrt{\gamma_e \cdot R_e \cdot T_e} \quad (12)$$

Where $\gamma_e = 1.1485$, $M = 24.468$ g/mol, and $R_e = \frac{8314.46}{24.468} \approx 339.8$ J/(kg·K). This yields:

$$v_e \approx 3542 \text{ m/s} \tag{13}$$

which closely matches the CEA value for effective exhaust velocity. Lastly, the specific impulse can be independently verified from equation (1) With $g_0 = 9.80665$ m/s^2, the result is:

$$I_{sp} \approx 361.7 \text{ s} \tag{14}$$

which aligns well with the expected performance characteristics.

Table 4: *Calculated parameters*

Parameter	Value	Unit
A_t (Throat Area)	461.3	cm^2
D_t (Throat Diameter)	242.4	mm
V_c (Chamber Volume)	41.52	dm^3
D_c (Chamber Diameter)	325	mm
A_c (Chamber Cross-sectional Area)	830	cm^2
A_e (Nozzle Exit Area)	15,840	cm^2
D_e (Nozzle Exit Diameter)	1420	mm
F (Thrust)	2.547	MN
c_e (Effective Exhaust Velocity)	3546.5	m/s
v_e (Exit Velocity)	3542	m/s
I_{sp} (Specific Impulse by Weight)	361.7	s

II.1.2 Design Using Rocket Propulsion Analysis (RPA)

Rocket Propulsion Analysis (RPA) is a specialized software tool used for the design and performance evaluation of rocket engines. It allows engineers to simulate and analyze thermodynamic processes in propulsion systems by solving complex chemical equilibrium and flow equations. With inputs such as propellant types, combustion chamber pressure, mixture ratio, and nozzle geometry, RPA provides key engine performance parameters like specific impulse, thrust, characteristic velocity (c^*), and thrust coefficient (C_F). In this study, RPA is utilized to refine the preliminary engine design, validate thermochemical results from NASA CEA, and optimize the nozzle geometry for improved performance under realistic conditions.



Figure 4: *RPA Logo*

Table 5: *RPA configuration parameters*

Parameter	Value	Unit	Source / Note
Chamber Pressure	300	bar	—
Mixture Ratio	Optimum	—	Optimized for maximum delivered I_{sp}
Expansion Area Ratio (A_e/A_t)	36	—	—
Ambient Pressure	1	atm	—
Engine Propellant Mass Flow Rate	718	kg/s	—
Chamber Length (L_c)	500	mm	—

To approximate the geometry of the Raptor 2 engine, particularly the nozzle exit diameter, the expansion area ratio was set to 36 instead of the nominal 34.34. This adjustment allowed RPA to compute an exit diameter close to 1300 mm, matching the real-world dimensions. Additionally, instead of imposing a fixed oxidizer-to-fuel ratio (O/F) such as 3.6, the O/F was set to "optimum" to let RPA determine the ratio that maximizes the specific impulse (Isp), ensuring performance-oriented sizing in this early design stage.

Table 6: *Combustion properties*

Parameter	Injector	Nozzle Throat	Nozzle Exit	Unit
Pressure	30.0000	17.3297	0.0862	MPa
Temperature	3791.3040	3593.8418	1925.0818	K
Gamma (γ)	1.1765	1.1683	1.1905	—
Gas Constant	0.3759	0.3714	0.3489	kJ/(kg·K)
Molecular Weight	22.1159	22.3857	23.8106	—
Density	21.0476	12.9828	0.1283	kg/m^3
Sonic Velocity	1273.3108	1230.4466	894.1698	m/s
Mach Number	0.0000	1.0000	3.8690	—

Table 7: *Engine performance*

Parameter	Sea Level	Optimum Expansion	Vacuum	Units
Characteristic Velocity	1877.9763	—	—	m/s
Effective Exhaust Velocity	3425.4853	3459.5782	3653.7437	m/s
Specific Impulse (by Mass)	3425.4853	3459.5782	3653.7437	N·s/kg
Specific Impulse (by Weight)	349.3023	352.7788	372.5782	s
Thrust Coefficient	1.8240	1.8422	1.9456	—
Thrust	2459.4985	2483.9771	2623.3880	kN
Altitude	0.0000	1.3435	—	km
Ambient Pressure	1.0000	0.8506	0.0000	atm

Table 8: *Chamber size parameters*

Parameter	Value	Unit
D_c	306.22	mm
D_t	217.47	mm
L_{cyl}	356.90	mm
L_c	500.00	mm
L^*	910.59	mm
R_1	163.10	mm
R_2	84.07	mm
b	30.00	deg
A_c/A_t	1.98	—

Table 9: *Nozzle size parameters*

Parameter	Value	Unit
Type	Parabolic nozzle	—
R_n	41.54	mm
T_n	32.34	deg
T_e	12.40	deg
D_e	1304.80	mm
L_e	1505.50	mm
L_e/D_t	6.92	—
L_e/L_{c15}	74.00	%
A_e/A_t	36.00	—

Table 10: *Mass flow and mixture ratio*

Parameter	Value	Unit
Mass Flow Rate (Total)	718.0000	kg/s
Mass Flow Rate (Oxidizer)	538.6327	kg/s
Mass Flow Rate (Fuel)	179.3673	kg/s
Oxidizer Excess Coefficient (α)	0.8492710	—
Mixture Ratio (O/F)	3.0029598	—
Stoichiometric O/F (O/F_0)	3.5359264	—

Table 11: *Combustion products composition*

Product	Injector Mass Frac.	Injector Mole Frac.	Throat Mass Frac.	Throat Mole Frac.	Exit Mass Frac.	Exit Mole Frac.
CO	0.2193531	0.1731943	0.2083401	0.1665059	0.1327135	0.1128161
CO_2	0.2734921	0.1374367	0.2908763	0.1479562	0.4098033	0.2217173
COOH	0.0000913	0.0000449	0.0000528	0.0000263	—	—
Co	0.0019975	0.0007496	0.0019979	0.0007589	0.0001873	0.0000757
Co(L)	0.0018112	0.0007318	—	—	—	—
Co^+	0.0000010	0.0000004	0.0000006	0.0000002	—	—
H	0.0007737	0.0169761	0.0006559	0.0145679	0.0000116	0.0002734
H_2	0.0066533	0.0729919	0.0062578	0.0694907	0.0059467	0.0702401
H_2O	0.4091088	0.5022295	0.4181202	0.5195550	0.4493610	0.5939160
H_2O_2	0.0000884	0.0000574	0.0000518	0.0000341	—	—
HCHO (Formaldehyde)	0.0000022	0.0000016	0.0000011	0.0000008	—	—
HCO	0.0000462	0.0000352	0.0000249	0.0000192	—	—
HCOOH	0.0000214	0.0000103	0.0000120	0.0000058	—	—
HO_2	0.0003410	0.0002285	0.0002082	0.0001412	—	—
O	0.0059450	0.0082177	0.0045469	0.0063618	0.0000004	0.0000006
O_2	0.0310470	0.0214580	0.0260298	0.0182100	0.0000029	0.0000021
O_3	0.0000007	0.0000003	0.0000003	0.0000001	—	—
OH	0.0510370	0.0663672	0.0428231	0.0563654	0.0001620	0.0002268
OH^-	0.0000002	0.0000003	0.0000001	0.0000001	—	—

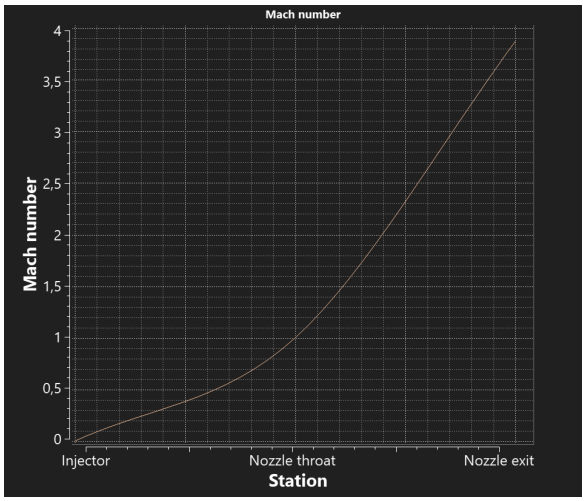


Figure 5: *Mach Number Distribution in RPA*

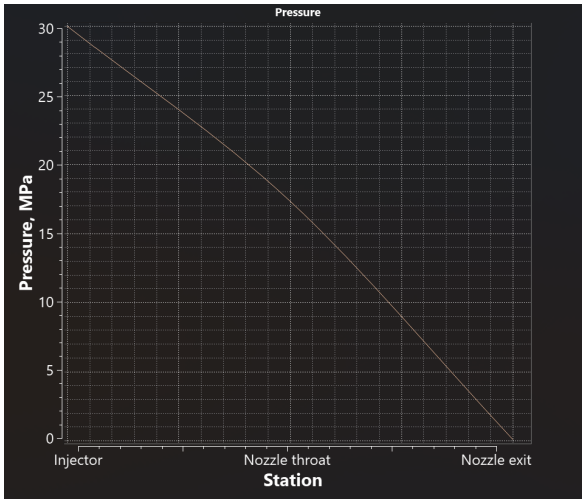


Figure 6: *Pressure Distribution in RPA*

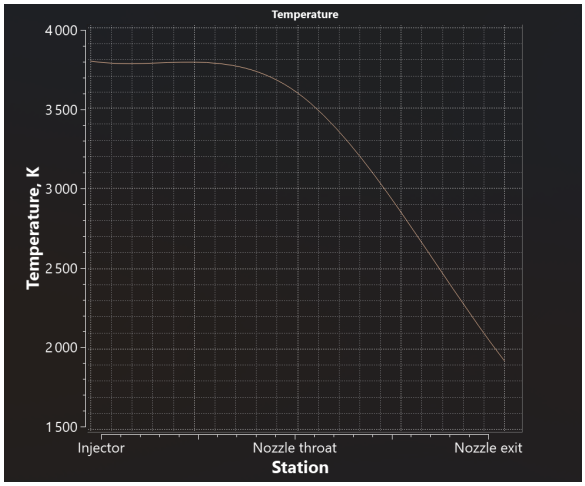


Figure 7: *Temperature Distribustion in RPA*

II.1.3 Comparison Between NASA CEA and RPA

To ensure the consistency and reliability of the propulsion parameters obtained in this study, a comparative analysis was performed between the results from the preliminary design phase (using NASA CEA outputs) and the refined results computed via Rocket Propulsion Analysis (RPA). This comparison focuses exclusively on sea level conditions, as this represents a critical operating point for engine performance evaluation, especially during launch.

The parameters compared include both performance characteristics and geometric aspects of the engine design. Performance-related variables such as Specific Impulse (I_{sp}), Thrust (F), Effective Exhaust Velocity (c_e), Thrust Coefficient (C_F), and Mach Number at the nozzle exit (M_e) are evaluated.

In addition, detailed fluid dynamic properties such as exit velocity (v_e), sonic velocity (at the combustion chamber, throat, and nozzle exit), pressure, and temperature across the same regions are also taken into account.

From a geometric perspective, the comparison involves critical design dimensions including the throat area (A_t), throat diameter (D_t), chamber volume (V_c), chamber diameter (D_c), chamber cross-sectional area (A_c), nozzle exit area (A_e), and nozzle exit diameter (D_e). These parameters directly affect the performance, cooling requirements, and structural integrity of the engine.

Furthermore, combustion product composition is also analyzed and compared. Differences in the predicted chemical species can influence the engine's thermal and chemical environment, which is essential for further CFD and heat transfer modeling.

This comprehensive comparison allows us to validate the preliminary assumptions made during the conceptual design phase, adjust the model accordingly, and ensure a more accurate and robust propulsion system design before proceeding to detailed simulations and structural analysis.

Table 12: *Comparison of performance parameters between RPA and NASA CEA results*

Parameter	RPA Result	NASA CEA Result	Difference	% Difference
Thrust (MN)	2.4	2.5	0.1	4.00%
Specific Impulse (I_{sp}) (s)	349	361	12	3.32%
Effective Exhaust Velocity (m/s)	3425	3546	121	3.41%
Thrust Coefficient (C_f)	1.8240	1.8416	0.0176	0.96%
Mach Number	3.8690	3.731	0.138	3.70%
Exit Velocity (m/s)	3459	3542	83	2.34%

Table 13: *Comparison of thermodynamic properties between RPA and NASA CEA results*

Parameter	Location	RPA	NASA CEA	Absolute Difference	Relative Error (%)
Pressure (MPa)	Chamber	30.0000	30.0000	0.0000	0.00%
	Throat	17.3297	17.333	0.0033	0.02%
	Nozzle Exit	0.0862	0.10063	0.0144	14.32%
Temperature (K)	Chamber	3791.30	3950.36	159.06	4.02%
	Throat	3593.84	3749.45	155.61	4.15%
	Nozzle Exit	1925.08	2315.23	390.15	16.85%
Density (kg/m^3)	Chamber	21.0476	20.015	1.0326	5.16%
	Throat	12.9828	12.349	0.6338	5.13%
	Nozzle Exit	0.1283	0.12791	0.00039	0.30%
Sonic Velocity (m/s)	Chamber	1273.31	1306.20	32.89	2.52%
	Throat	1230.45	1261.50	31.05	2.46%
	Nozzle Exit	894.17	950.60	56.43	5.93%

Table 14: *Comparison of geometric parameters between RPA and NASA CEA results*

Parameter	RPA Result (mm)	NASA CEA-Based Design (mm)	Difference (mm)	Relative Error (%)
Throat Diameter (D_t)	217.47	242.4	+24.93	**+11.47%**
Chamber Diameter (D_c)	306.22	325	+18.78	**+6.13%**
Nozzle Exit Diameter (D_e)	1304.80	1420	+115.20	**+8.83%**

Table 15: *Comparison of combustion product mass fractions between RPA and NASA CEA results*

Species	Location	NASA CEA	RPA	Difference	Relative Error (%)
CO	Chamber	0.21735	0.21935	+0.00200	+0.92%
	Throat	0.20581	0.20834	+0.00253	+1.23%
	Exit	0.10507	0.13271	+0.02764	+26.3%
CO_2	Chamber	0.25467	0.27349	+0.01882	+7.39%
	Throat	0.27289	0.29088	+0.01799	+6.59%
	Exit	0.43129	0.40980	-0.02149	-4.98%
H_2O	Chamber	0.38360	0.40911	+0.02551	+6.65%
	Throat	0.39362	0.41812	+0.02450	+6.23%
	Exit	0.45454	0.44936	-0.00518	-1.14%
H_2	Chamber	0.00650	0.00665	+0.00015	+2.31%
	Throat	0.00606	0.00626	+0.00020	+3.30%
	Exit	0.00345	0.00595	+0.00250	+72.5%
O_2	Chamber	0.05496	0.03105	-0.02391	-43.5%
	Throat	0.05002	0.02603	-0.02399	-47.9%
	Exit	0.00144	∼0.000003	∼-0.00144	∼-99.8%
OH	Chamber	0.06994	0.05104	-0.01890	-27.0%
	Throat	0.06109	0.04282	-0.01827	-29.9%
	Exit	0.00401	0.000162	-0.00385	-96.0%
O	Chamber	0.01104	0.00595	-0.00509	-46.1%
	Throat	0.00904	0.00455	-0.00449	-49.7%
	Exit	0.00012	∼0.00000	-0.00012	∼-100%

This comparative study between NASA CEA and RPA has provided valuable insight into the performance and reliability of both tools in modeling rocket engine thermodynamics and geometry.

The thrust (F), specific impulse (I_{sp}), and exit velocity (v_e) predicted by NASA CEA are slightly higher, which can be attributed to its idealized equilibrium assumptions. In contrast, RPA delivers results that are slightly more conservative yet highly consistent, making it particularly suitable for engineering design applications. The observed differences, while present, remain within acceptable margins for conceptual and preliminary design stages.

When analyzing the flow characteristics, RPA predicts a higher Mach number (M_e), indicating a potentially stronger expansion or more realistic modeling of acceleration in the nozzle. However, key parameters such as the coefficient of thrust (C_f) and effective exhaust velocity (c_e) remain closely matched, confirming the compatibility of both tools in evaluating propulsion performance.

From a thermodynamic standpoint, chamber and throat pressures are nearly identical, but temperature differences especially at the nozzle exit (∼16.85%) highlight variations in how each tool handles expansion and combustion efficiency. Density (ρ) and sonic velocity (a) discrepancies are minor (∼5% or less), which further reinforces the reliability of both models, though caution is advised when transitioning to detailed simulations or experimental validation.

In terms of geometric design, differences in throat (D_t), chamber (D_c), and exit diameters (D_e) were observed (up to ∼11.5%), mainly due to differing modeling approaches: NASA CEA follows idealized design correlations, while RPA uses iterative solving with detailed chemistry and flow modeling.

These deviations underline the importance of refining preliminary geometries using high-fidelity tools like RPA during the post-design phase.

The chemical composition analysis revealed that major species (CO_2, H_2O) are in strong agreement between both tools (within ∼5–7%), confirming that core combustion products are consistently predicted. However, discrepancies in minor species (H, H_2, OH, O, O_2) especially at the exit, are more prominent. This is likely due to how each code handles dissociation, recombination, and flow freezing during expansion, which becomes critical in CFD analysis and plume modeling.

II.1.4 Geometry Visualization

We use SolidWorks to create the geometry based on the output results provided by RPA. Since the problem is axisymmetric, we do not use a full 3D model to simplify the simulation. Instead, we build a 2D axisymmetric model, which significantly reduces computational cost while preserving accuracy for this type of flow. The injectors are simplified and dimensioned according to approximated sizing methods, sufficient for the purposes of the simulation.

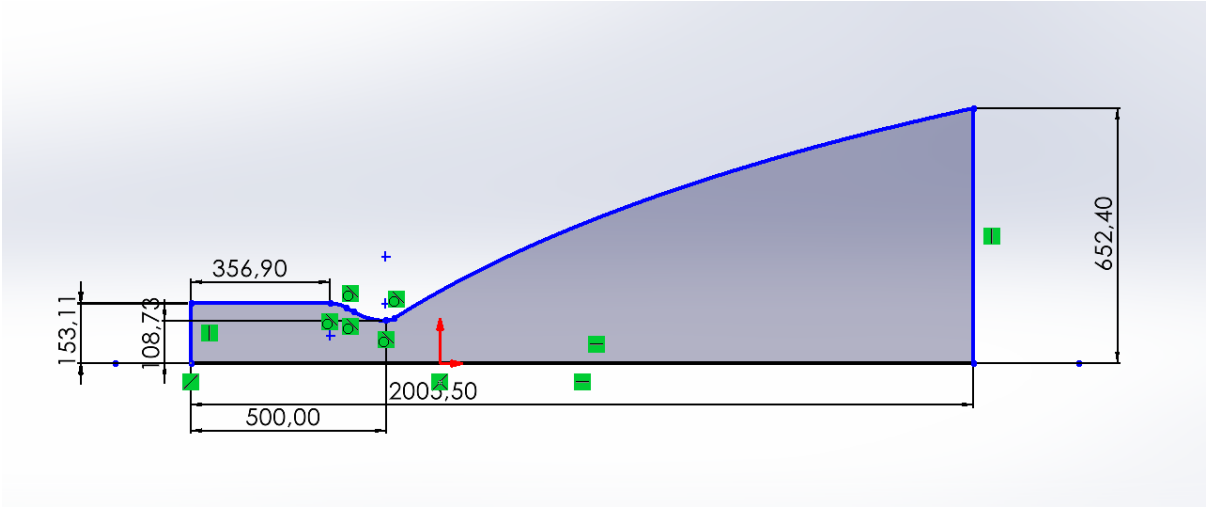


Figure 8: *Raptor 2 Sketch*

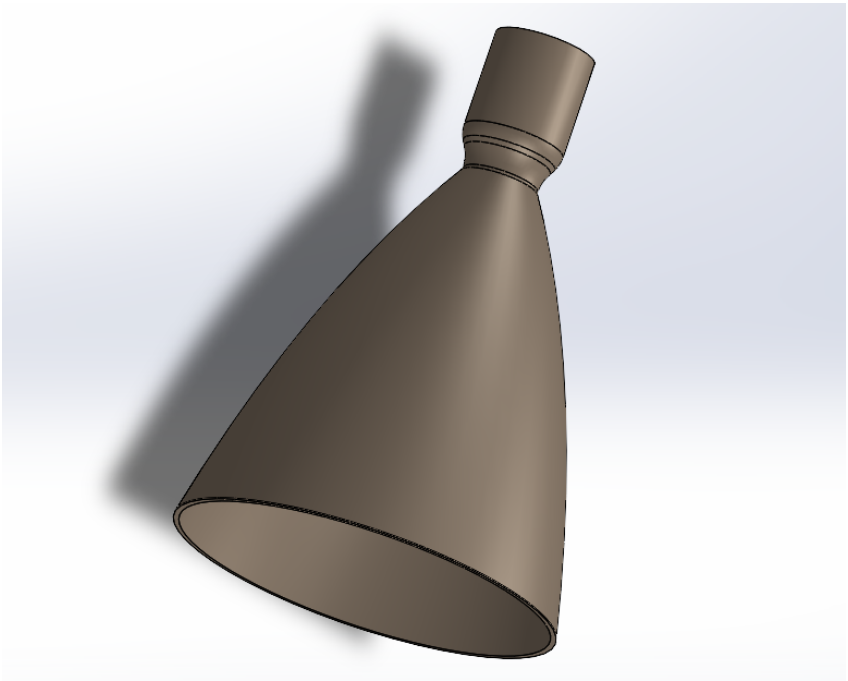


Figure 9: *Raptor 2 3D Inner Wall*

II.1.5 Sizing the Injectors

3D injectors :

The sizing of the injectors is a critical aspect of the injector plate design. In our case, we began with the total number of injectors, which is 640, and distributed the overall propellant flow between oxidizer and fuel according to the mixture ratio. Using the total mass flow rate and assuming uniform flow distribution, we calculated the total flow area required for each propellant. From this, we derived the area of a single injector orifice for the oxidizer and fuel, respectively.

These values were then used to dimension the injector holes and ensure consistency with the global mass flow requirements imposed by the engine design parameters.

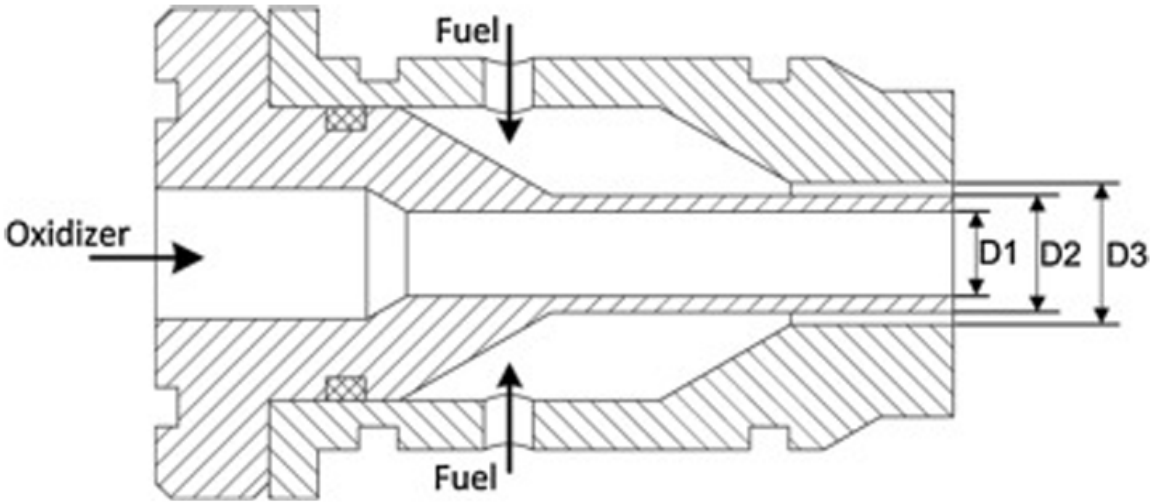


Figure 10: *Coaxial Injector Gemetry*

Pressure drop across the injectors A significant drop in static pressure across the injector orifices is essential to prevent combustion chamber pressure fluctuations from propagating upstream into the propellant feed system an effect that could trigger dangerous instabilities. This requirement becomes even more critical as the propellant mass flow rate increases. The magnitude of the pressure drop depends not only on throttling but also on the detailed geometry of the injectors. For throttled engines, the pressure drop typically ranges between 20% and 30% of the combustion chamber pressure.

Considering the distinct geometries of the oxidizer and fuel orifices, as well as their differing mass flow rates, the resulting pressure drops in our case are:

$$\text{Oxidizer } (\Delta P_{O_2}) :\approx 24\% \tag{15}$$

$$\text{Fuel } (\Delta P_{CH_4}) :\approx 9.5\% \tag{16}$$

relative to the combustion chamber pressure, which is 300 bar.

This disparity in pressure loss is primarily due to the fact that the oxidizer is injected with a swirling motion, which increases resistance, while the fuel is injected without swirl a choice often made for simplicity and cost-effectiveness. Additionally, historical data and industry practices consistently show that oxidizer injectors tend to have higher pressure losses compared to fuel injectors, further validating our computed values.

Table 16: *Thrust chamber injectors pressure losses*

Parameter	LOX	CH_4
ΔP [bar]	72.2	28.8

Discharge coefficient One of the key factors influencing the injector pressure drop is the discharge coefficient (C_d). In this study, a value of 0.6 was selected for both the oxidizer and fuel injector orifices.

This choice was based on a comparison between the coaxial swirl injector geometry used here and other commonly studied injector configurations of similar diameter, such as short tubes with spiral flow and sharp-edged conical inlets. Despite geometric differences, these configurations exhibit comparable flow behavior, justifying the selected C_d value as a representative estimate for the expected flow resistance.

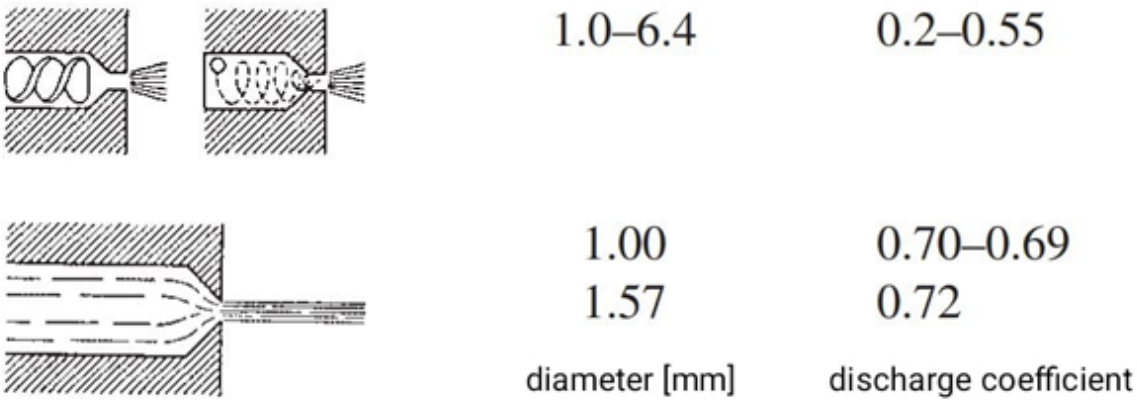


Figure 11: *Discharge coefficient*

Propellant density In this analysis, the propellants entering the combustion chamber are not pure substances but gas mixtures exiting their respective preburners. The fuel stream (fuel-rich preburner) contains a mixture dominated by methane with combustion byproducts, while the oxidizer stream (oxidizer-rich preburner) is primarily composed of oxygen with similar byproducts. To determine the density of each mixture at the injector inlet, the ideal gas law is applied using a mass-fraction-weighted average molar mass for each stream.

The governing equation is:

$$\rho = \frac{P \cdot \bar{M}}{R_u \cdot T} \tag{17}$$

From Table 2, we can extract the mass fractions of each species in both the fuel and oxidizer streams. Using the formula:

$$\bar{M}_{\text{fuel}} = \sum (Y_i \cdot M_i) \tag{18}$$

we obtain:

For the fuel mixture:

$$\bar{M}_{\text{fuel}} = 0.01907\,\text{kg/mol}$$

For the oxidizer mixture:

$$\bar{M}_{\text{ox}} = 0.03204\,\text{kg/mol}$$

Given:

Fuel:

$$T = 811\,\text{K},\ P = 300\,\text{bar}$$

Oxidizer:

$$T = 748\,\text{K},\ P = 300\,\text{bar}$$

Fuel-side Density:

$$\rho_{\text{fuel}} = \frac{3.0 \times 10^7 \cdot 0.01907}{8.314 \cdot 811} \approx 84.79\,\text{kg/m}^3 \tag{19}$$

Oxidizer-side Density:

$$\rho_{\text{ox}} = \frac{3.0 \times 10^7 \cdot 0.03204}{8.314 \cdot 748} \approx 154.54\,\text{kg/m}^3 \tag{20}$$

Table 17: *Density of Propellant Before Injection*

Mixture	Molar Mass (kg/mol)	Density (kg/m^3)
Fuel	0.01907	84.79
Oxidizer	0.03204	154.54

Sizing Using the given data, along with the known values of discharge coefficients, pressure drops, and fluid densities, it is now possible to calculate the total injection area for both the oxidizer and the fuel. The total injection area A_{tot} is determined using the following formula:

$$A_{\text{tot}} = \frac{\dot{m}}{C_d \sqrt{2\rho\Delta P}} \tag{21}$$

Once the total injection area is known, and given the number of injector elements (640), the injection area per orifice can be calculated.

From this, the diameter of each orifice can be derived using:

$$N = \frac{A_{\text{tot}}}{A_{\text{si}}} \tag{22}$$

where:

- N is the number of injectors,
- A_{si} is the area of a single injector orifice.

After calculation we found the next results

Table 18: *Injection Areas for Oxidizer and Fuel*

Parameter	Oxidizer	Fuel
A_{tot} (cm^2)	198.63	116.90
A_{si} (mm^2)	31.04	18.26

Table 19: *Injector Diameters: Maximum vs Chosen*

Parameter	Max (mm)	Chosen (mm)
D_1	6.29	6.0
D_2	7.00	7.0
D_3	8.50	8.5

Table 20: *Final Propellants Areas*

Parameter	Oxidizer	Fuel
A_{sis} (mm^2)	28.27	18.26
A_{tot} (cm^2)	180.95	116.86

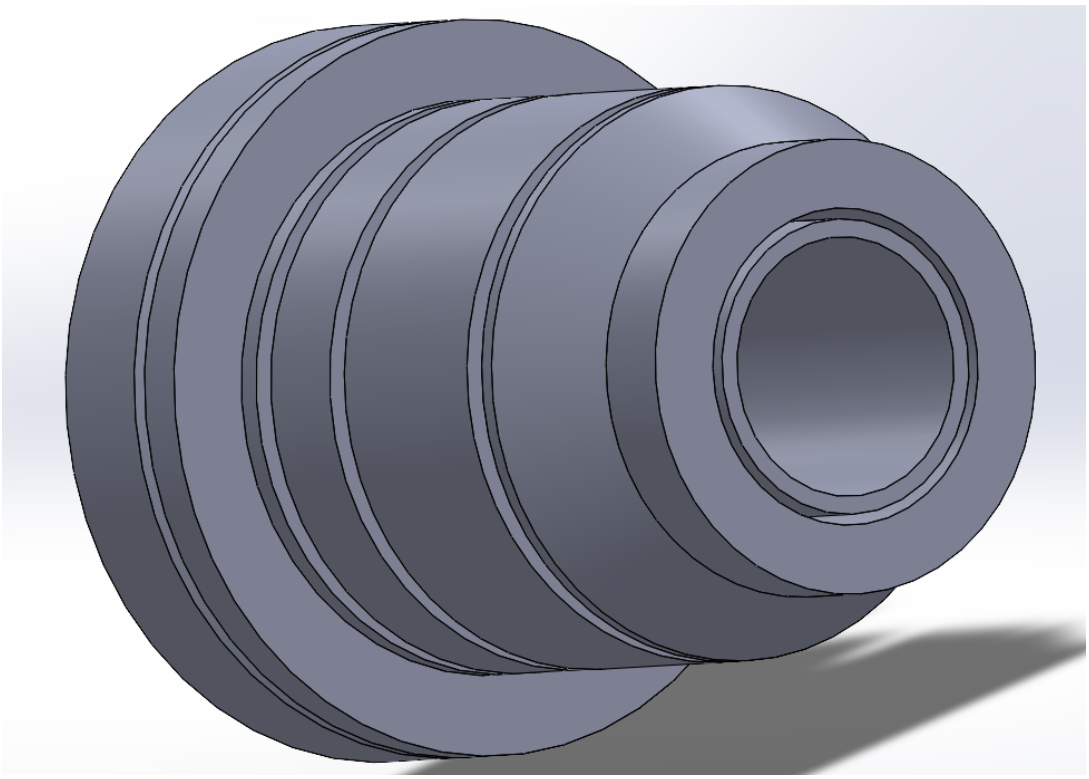


Figure 12: *Injector Geometry*

2D injectors :

In our simulation, as we said we chose to run a 2D axisymmetric model since the overall geometry of the problem is axisymmetric. However, this symmetry does not apply to the injectors, which are inherently non-axisymmetric. This suggests that we should implement simplified 2D representations of the injectors within our simulation. Doing so will enhance the accuracy and reliability of the results.

To properly model the injection in our 2D axisymmetric simulation, we first need to calculate the linear mass flow rate using the following relation:

$$\dot{m}' = \frac{\dot{m}}{2\pi r_c} \tag{23}$$

where:

- $\dot{m}'$ is the linear mass flow rate [kg/(sm)],
- $\dot{m}$ is the total mass flow rate from Table 1 [$\mathrm{kg\,s^{-1}}$],
- r_c is the radius of the combustion chamber from Table 8 [m].

Next, we calculate the total linear injection length L_{tot} using:

$$L_{\text{tot}} = \frac{\dot{m}'}{C_d\sqrt{2\rho\Delta P}} \tag{24}$$

Finally, we compute the individual injector length L_{sis} by dividing the total injection length by the number of injectors used in the 2D simulation:

$$L_{\text{sis}} = \frac{L_{\text{tot}}}{N} \tag{25}$$

In our case, we are modeling 10 injectors, so $N = 10$.

After Calculation we found the next results

Table 21: *Injector flow parameters*

Parameter	Oxidizer	Fuel
$\dot{m}$ (kg/s)	563	155
$\dot{m}'$ (kg/(s·m))	585.22	161.11
L_{tot} (mm)	20.64	12.15
L_{sis} (mm)	2.06	1.21

Table 22: *Injector length parameters*

Parameter	Max	Chosen
L_1 (mm)	2.06	2
L_2 (mm)	3	3
L_3 (mm)	4.21	4.2

In our 2D axisymmetric model, we will represent 10 injectors. Each injector has a length of 4.2 mm, and the center-to-center spacing between adjacent injectors is 10.58 mm. The radial distance from the injector center to the axis of symmetry is 5.29 mm.

Each injector consists of:

- One oxidizer inlet with a length of 2 mm
- Two fuel inlets, each with a length of 0.6 mm

The spacing between the fuel and oxidizer inlets is 0.5 mm.

II.2 Meshing

For the meshing process, we used face meshing with quadrilateral elements. A size division method was applied to each edge to control the mesh density. The following table summarizes the number of divisions used for each edge:

Table 23: *Mesh divisions configuration*

Edge	Number of Divisions
Inlet – Fuel	2
Inlet – Oxidizer	6
Spacing Between Inlets	1
Spacing Between Injectors	10
Throat	130
Outlet	100
Axis / Wall	260

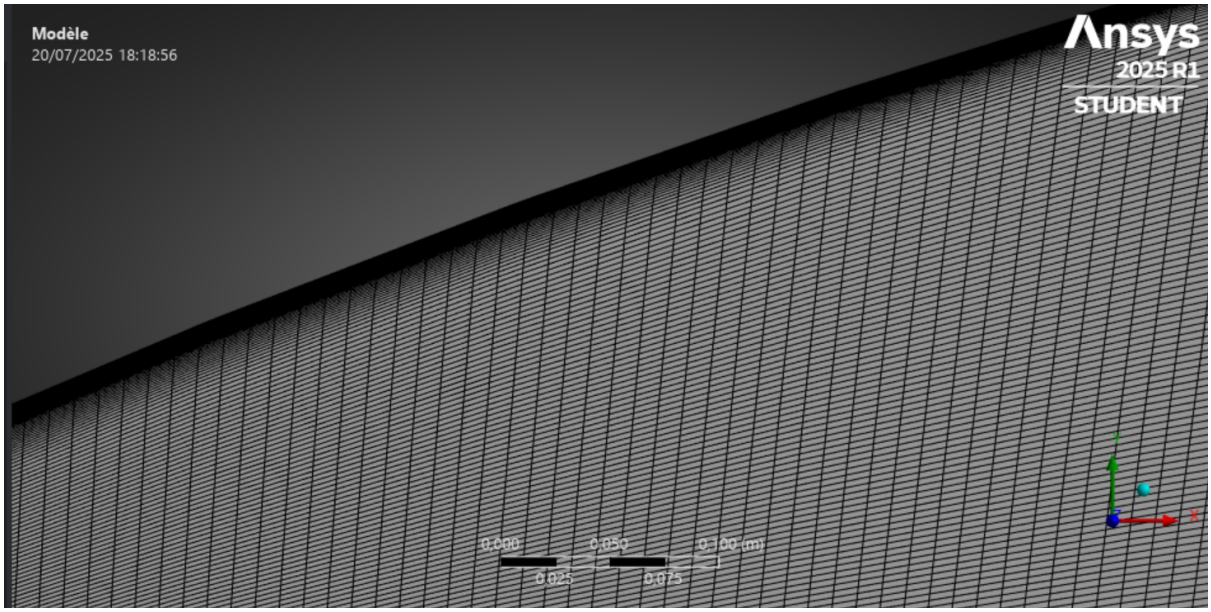


Figure 13: *Mesh Near the Wall*

To accurately capture viscous effects, we refined the mesh near the wall by applying 20 divisions along the wall boundaries, enhancing resolution in the boundary layer region.

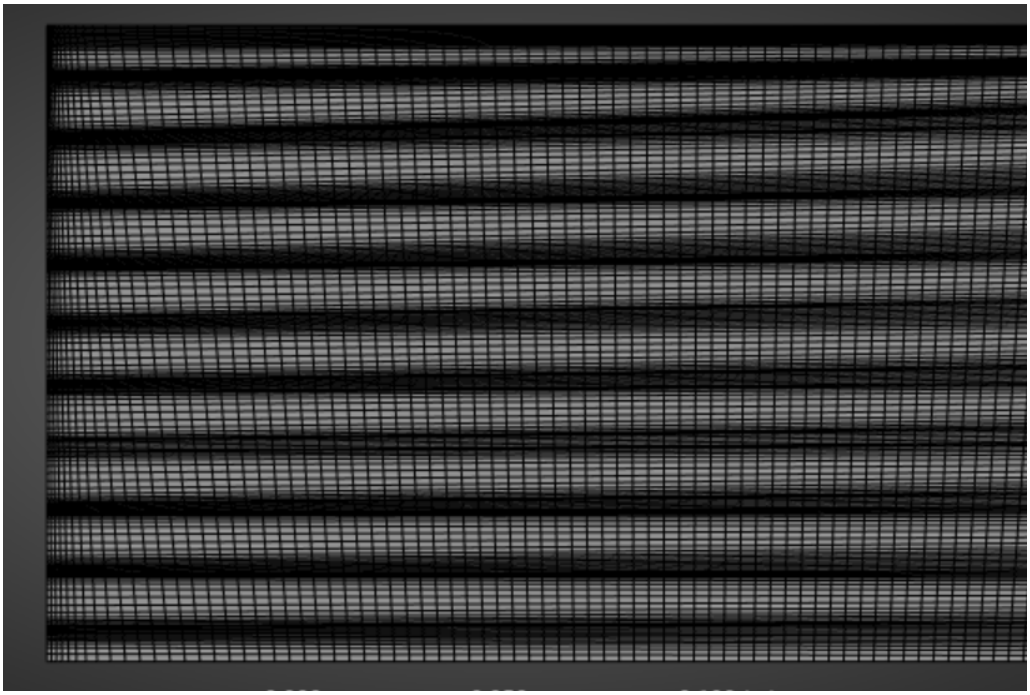


Figure 14: *Mesh in the Combustion Chamber*

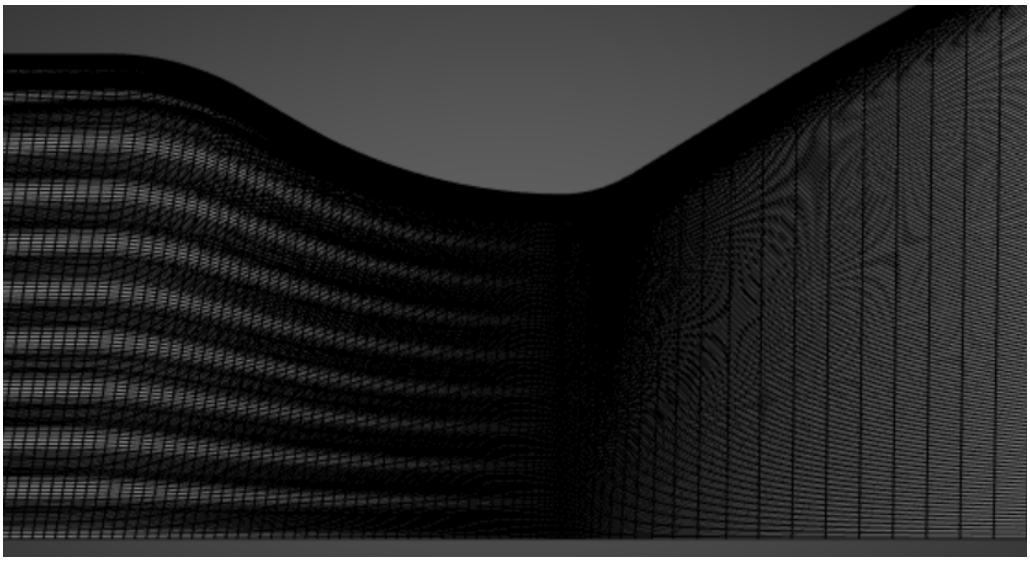


Figure 15: *Mesh in the Throat*

II.3 Boundary conditions

To accurately simulate the internal flow and combustion dynamics within the Raptor 2 combustion chamber and nozzle, it is essential to define appropriate boundary conditions for the fundamental conservation equations of mass, momentum, energy, and species. The boundary conditions used in the current study are described as follows.

Inlets:

For the inlet boundary conditions, the mass flow rates of the fuel and oxidizer are initially set according to the optimal values obtained from RPA (Rocket Propulsion Analysis) results, as presented in Table 10. These are used in the first simulation to provide a baseline comparison.

To investigate the effects of the Full-Flow Staged Combustion (FFSC) cycle, three separate simulations are carried out:

- **Simulation 1 : Liquid Propellants**: Pure liquid methane (CH_4) and liquid oxygen (O_2) are used at an inlet temperature of 180 K and 90 K for Fuel and Oxidizer.
- **Simulation 2 : Gaseous Propellants**: Pure gaseous CH_4 and O_2 are injected, with inlet temperatures specified in Table 1. This setup represents a simplified approximation of preburned gases entering the main combustion chamber.
- **Simulation 3 : Realistic Mass Fractions**: Realistic mass fractions of oxidizer and fuel, derived from the FFSC configuration (see Table 2), are used with temperatures as specified in Table 1. This configuration provides a more accurate representation of actual engine conditions.

In all simulations, turbulent intensity is set to 10% at the fuel inlets to reflect the swirling motion characteristic of such injectors and 5% at the oxidizer inlets.

Outlet:

For the outlet boundary condition, two pressure outlet configurations are considered:

- In the first 4 simulations, the outlet gauge pressure is set to 0 atm to replicate vacuum conditions and enable direct comparison with RPA results.
- In the final 4 simulations, the outlet gauge pressure is set to 1 atm to assess engine performance in sea-level conditions and evaluate the gain in specific impulse.

Walls:

All internal walls are treated with a no-slip boundary condition. In the initial modeling approach, the walls are assumed to be adiabatic for computational simplicity, implying zero heat flux. Chemical reactions at the wall surface are neglected, and the walls are considered non-reactive.

Axis:

An axisymmetric boundary condition is applied along the engine's central axis to model the two-dimensional axisymmetric nature of the geometry and flow.

Table 24: *Simulation boundary conditions*

Parameter	1st	2nd	3rd	4th	5th	6th	7th	8th
O/F	3	3.6	3.6	3.6	3	3.6	3.6	3.6
Nature of Chemicals	Real Fraction	Pure	Pure	Real Fraction	Real Fraction	Pure	Pure	Real Fraction
Fuel Inlet Temp. (K)	808	180	808	808	808	180	808	808
Oxidizer Inlet Temp. (K)	707	90	707	707	707	90	707	707
Gauge Pressure (atm)	0	0	0	0	1	1	1	1

II.4 Governing equations

The mathematical model employed in this study is based on the steady-state conservation equations of mass, momentum, energy, and species. Given the highly turbulent and reactive environment inside the combustion chamber and nozzle, the following modeling strategies are adopted:

- Reynolds-Averaged Navier-Stokes (RANS) equations are used to model turbulence.
- Favre-averaging is applied to account for compressibility effects induced by high temperatures from combustion.
- Gravitational forces are neglected, as they are insignificant compared to pressure and inertial forces.
- Non-adiabatic, non-premixed combustion modeling is applied to simulate chemical reactions with heat release.

Notation:

- $\bar{y}$: Time-averaged value of a variable y
- $\tilde{y}$: Favre (density-weighted) average of y
- ρ: Density

Continuity Equation

$$\frac{\partial(\bar{\rho}\tilde{u}_i)}{\partial x_i} = 0 \tag{26}$$

This equation ensures conservation of mass. It states that the net mass flux entering and exiting a control volume is zero under steady-state conditions.

Momentum Conservation (i-Direction)

$$\frac{\partial(\bar{\rho}\tilde{u}_i\tilde{u}_j)}{\partial x_j} = -\frac{\partial \bar{p}}{\partial x_i} + \frac{\partial}{\partial x_j}\left(\mu\frac{\partial \tilde{u}_i}{\partial x_j}\right) - \frac{\partial}{\partial x_j}(\rho u_i'' u_j'') \tag{27}$$

$\tilde{u}_i$	Favre-averaged velocity component
$\bar{p}$	Mean pressure
μ	Molecular dynamic viscosity
$\rho u_i'' u_j''$	Reynolds stress tensor

To close this equation, the Reynolds stress term is modeled using the k-ω SST turbulence model, resulting in:

$$\frac{\partial(\bar{\rho}\tilde{u}_i\tilde{u}_j)}{\partial x_j} = -\frac{\partial}{\partial x_i}\left(\bar{p} + \frac{2}{3}\bar{\rho}\bar{k}\right) + \frac{\partial}{\partial x_j}\left[(\mu + \mu_t)\frac{\partial \tilde{u}_i}{\partial x_j}\right] \tag{28}$$

$\bar{k}$	Turbulent kinetic energy
μ_t	Eddy (turbulent) viscosity

Energy Conservation

$$\nabla \cdot (\bar{\rho}\tilde{\vec{v}}\tilde{H}) = \nabla \cdot \left(\frac{k_t}{C_p}\nabla \tilde{H}\right) + \bar{S}_h \tag{29}$$

$\tilde{H}$	Total enthalpy of the mixture
k_t	Turbulent thermal conductivity
C_p	Specific heat at constant pressure
$\bar{S}_h$	Viscous dissipation source term

Note: A unity Lewis number ($Le = 1$) is assumed, implying thermal and mass diffusivities are equal.

The total enthalpy H of the mixture is computed as:

$$H = \sum_j Y_j H_j \quad \text{with} \quad H_j = h_j^0(T_{ref}) + \int_{T_{ref}}^{T} C_{p,j} dT \tag{30}$$

Y_j	Mass fraction of species j
H_j	Specific enthalpy of species j
$h_j^0(T_{ref})$	Standard formation enthalpy
$C_{p,j}$	Specific heat of species j

Species Conservation

$$\nabla \cdot (\bar{\rho}\tilde{\vec{v}}\tilde{Y}_j) = -\nabla \cdot \tilde{\vec{J}}_j + \tilde{R}_j \tag{31}$$

$\tilde{Y}_j$	Favre-averaged mass fraction
$\tilde{\vec{J}}_j$	Diffusion flux of species j
$\tilde{R}_j$	Net rate of production/consumption

The diffusion flux is modeled in Ansys Fluent as:

$$\vec{J}_j = -\left(\rho D_{j,m} + \frac{\mu_t}{Sc_t}\right)\nabla Y_j - D_{T,j}\frac{\nabla T}{T} \tag{32}$$

$D_{j,m}$	Mass diffusion coefficient
μ_t	Turbulent viscosity
Sc_t	Turbulent Schmidt number
$D_{T,j}$	Thermal diffusion coefficient
$\nabla T/T$	Temperature gradient term

II.5 Modeling of Combustion

The equations presented earlier involve density-weighted average quantities, which are denoted by the tilde symbol ($\sim$). These averages are used in turbulent combustion modeling to account for fluctuations in properties such as species concentration or temperature. To compute these quantities, we adopt the Probability Density Function (PDF) approach.

In combustion modeling, a PDF is a mathematical tool that represents the statistical distribution of a variable such as temperature, species mass fractions, or reaction rates within the turbulent flow. Instead of calculating exact values at every point, we describe how these variables are spread or fluctuating due to turbulence, mixing, and chemical reactions.

In our case, the combustion model is coupled with a presumed PDF, specifically a beta distribution, which is widely used due to its flexibility and bounded support in [0,1]. This beta PDF is used to describe the distribution of the mixture fraction (ξ), a scalar quantity representing the local composition of the fuel-oxidizer mixture in the combustion chamber. A mixture fraction of $\xi = 0$ corresponds to pure oxidizer, while $\xi = 1$ represents pure fuel.

To compute the density-weighted average of a species mass fraction $\widetilde{Y}_i$, we use the following integral:

$$\widetilde{Y}_i = \int_0^1 Y_i(\xi)\widetilde{P}(\xi)d\xi \tag{33}$$

Where:

- $Y_i(\xi)$: The local mass fraction of species i as a function of the mixture fraction ξ
- $\widetilde{P}(\xi)$: The density-weighted probability density function

This density-weighted PDF $\widetilde{P}(\xi)$ is defined as:

$$\widetilde{P}(\xi) = \frac{\rho(\xi)}{\bar{\rho}}P(\xi) \tag{34}$$

Where:

- $\rho(\xi)$: The local density corresponding to the mixture fraction ξ
- $\bar{\rho}$: The mean density over the entire domain
- $P(\xi)$: The presumed (beta) PDF

This approach allows us to model the effect of turbulent fluctuations in combustion processes without resolving every turbulent eddy, which would be computationally expensive. Instead, by integrating over the PDF, we obtain more realistic average values of combustion variables such as species concentration and temperature.

II.6 Chemical kinetics and Thermochemistry properties

The chemical kinetics used in the CFD model are based on the GRI-Mech chemical kinetics database. GRI-Mech is a widely recognized mechanism that provides a detailed list of elementary chemical reactions and their corresponding rate constants. Specifically, it includes 53 chemical species and 325 reactions, making it suitable for accurately simulating combustion processes involving methane. This database is particularly chosen because it is optimized for methane fuel, which aligns with the needs of this study.

The reaction rate for each elementary chemical reaction in GRI-Mech follows the Arrhenius law, which is mathematically expressed as:

$$k_f = AT^n \exp\left(-\frac{E_a}{T}\right) \tag{35}$$

Where:

- k_f: Forward reaction rate coefficient [units depend on reaction order]
- A: Pre-exponential factor [s^{-1}] (collision frequency)
- T: Temperature [K]
- n: Temperature exponent (dimensionless)
- E_a: Activation energy [$J\,mol^{-1}$]
- $\exp\left(-\frac{E_a}{T}\right)$: Boltzmann factor (temperature dependence)

This formulation allows the model to account for the effect of temperature on reaction rates, which is crucial for accurately simulating the dynamics of combustion in high-temperature environments such as rocket engines.

The thermodynamic and chemical properties of all species are sourced from the database integrated with the GRI-Mech chemical kinetics mechanism.

II.7 Solver settings

We perform a steady-state simulation using the SIMPLE algorithm for the pressure-velocity coupling scheme. For spatial discretization, the Second Order Upwind method is applied to improve the accuracy of the solution.

To aid convergence, under-relaxation factors listed in Table 25 are used. Additionally, the following report definitions are monitored to ensure proper convergence:

- Mass flow rate
- Mach number at the outlet
- Velocity at the outlet
- Temperature at the outlet
- Pressure at the outlet

We use Standard Initialization with the initial values presented in Table 26.

Table 25: *Under-Relaxation Factors*

Parameter	Value
Pressure	0.3
Density	0.3
Body Forces	0.5
Momentum	0.1
Turbulent Kinetic Energy	0.4
Specific Dissipation Rate	0.4
Turbulent Viscosity	0.5
Energy	0.5
Temperature	0.5
Mean Mixture Fraction	0.5
Mixture Fraction Variance	0.5

Table 26: *Initial Values*

Parameter	Value
Gauge Pressure [Pa]	0
Axial Velocity [m/s]	256
Radial Velocity [m/s]	0
Turbulent Kinetic Energy [m^2/s^2]	585
Specific Dissipation Rate [1/s]	1365
Temperature [K]	3900
Mean Mixture Fraction	0.235
Mixture Fraction Variance	0

III Results

III.1 Convergence analysis

The simulation was executed for 5,000 iterations, after which convergence was reached.

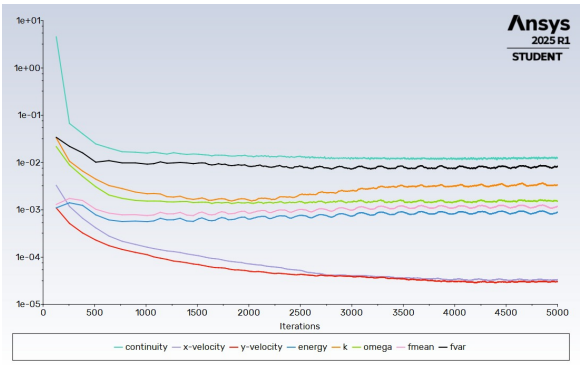


Figure 16: *Residuals in Function of Iterations*

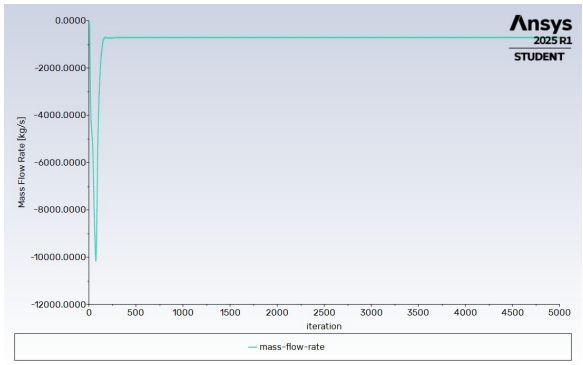


Figure 17: *Mass Flow Rate in Function of Iterations*

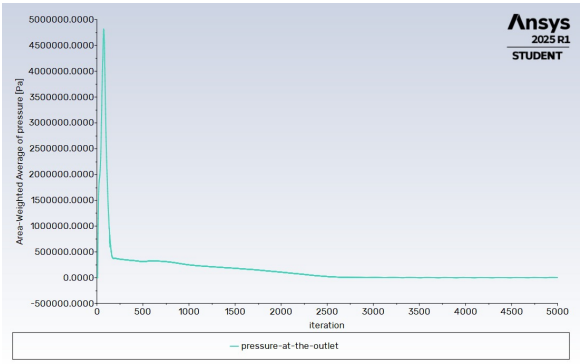


Figure 18: *Pressure at the Outlet in Function of Iterations*

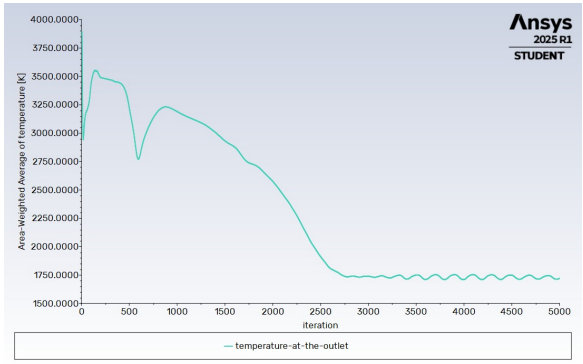


Figure 19: *Temperature at the Outlet in Function of Iterations*

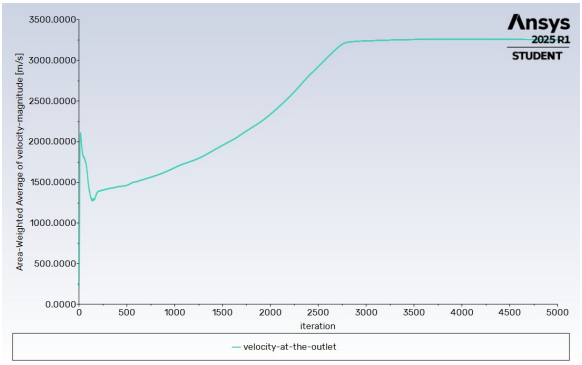


Figure 20: *Velocity at the Outlet in Function of Iterations*

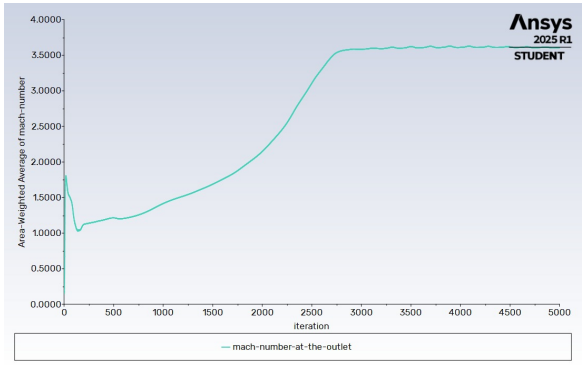


Figure 21: *Mach Number at the Outlet in Function of Iterations*

In practice, the simulation was run for 5000 iterations. Although the residuals of continuity did not fall below the typical convergence threshold of 1×10^{-3}, the residuals of other variables showed stable convergence. Additionally, the outlet temperature exhibited minor oscillations but remained within an acceptable range, indicating that the solution was not diverging and still physically meaningful.

It is common in complex reactive flows for certain residuals, such as continuity, to fluctuate or settle above strict thresholds while the key physical quantities stabilize. Moreover, the mass flow rate at the outlet reached -718 kg/s, which is consistent with the defined boundary condition, confirming that the imposed mass flow is correctly captured and the direction is outward as expected. These observations justify stopping the simulation at 5000 iterations, as the solution meets physical and numerical consistency.

III.2 Pressure

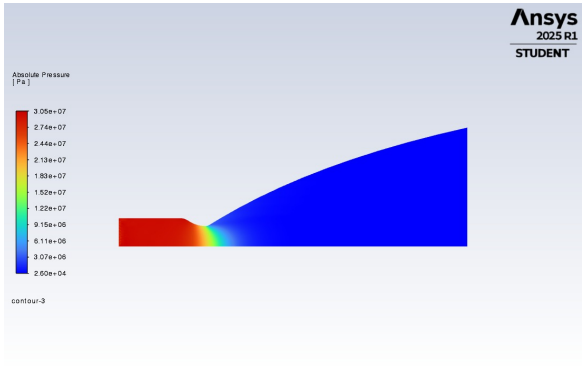


Figure 22: *Pressure Distribution*

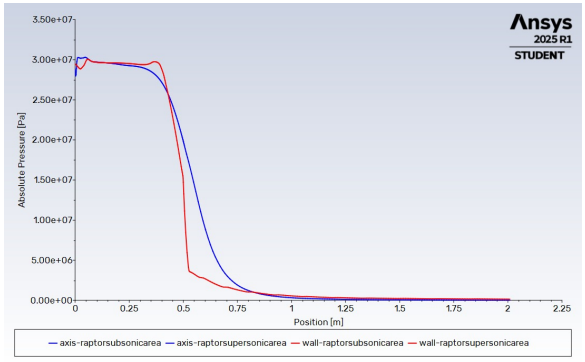


Figure 23: *Pressure in the wall in and in the axis*

In our simulation, the pressure recorded within the combustion chamber is approximately 305 bar. According to the technical specifications of the Raptor engine (see Table 1), the expected chamber pressure is around 300 bar. This slight difference of about 1.7% indicates a strong correlation between our numerical results and the actual engine data.

The pressure rise is a result of the combustion process, where high-speed injection and elevated temperatures lead to rapid energy release and expansion of gases. Inside the chamber, the pressure remains relatively stable with minor losses due to mixing and combustion inefficiencies.

As the hot gases pass through the convergent-divergent nozzle, the high chamber pressure is gradually converted into kinetic energy, resulting in a significant pressure drop along the nozzle profile. This distribution confirms the physical behavior expected in a high-performance rocket engine and validates the reliability of our simulation setup.

III.3 Temperature

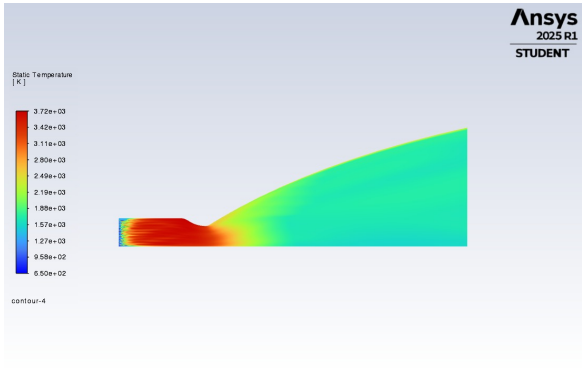


Figure 24: *Temperature Distribution*

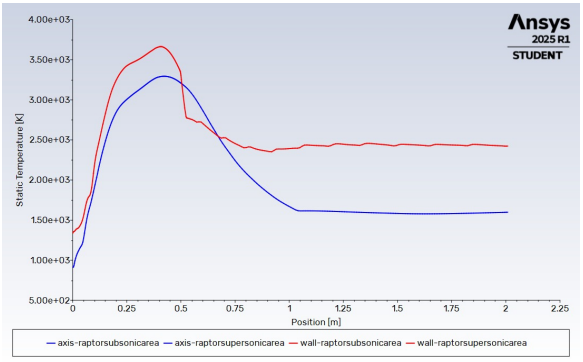


Figure 25: *Temperature in the wall in and in the axis*

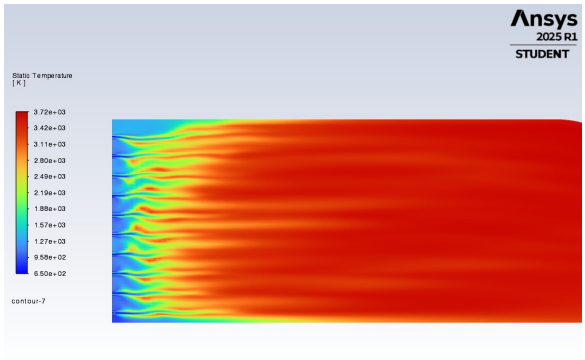


Figure 26: *Temperature Distribution zoom in the Combustion Chamber*

In our simulation, the temperature within the combustion chamber reaches a peak of approximately 3720 K. This rise in temperature is the result of the combustion reaction between the injected fuel and oxidizer, which mix and ignite inside the chamber. The elevated temperature confirms that the combustion process has occurred efficiently. After combustion, the hot gases expand and enter the convergent-divergent nozzle, where part of their internal energy is converted into kinetic energy. As a result, a significant temperature drop is observed along the nozzle profile. The obtained temperature aligns well with typical values reported for methane-oxygen combustion under high-pressure conditions. The adiabatic behavior assumed in the model neglecting heat loss through chamber walls naturally leads to higher gas temperatures than in real engines, where regenerative cooling is employed to prevent thermal damage.

III.4 Velocity

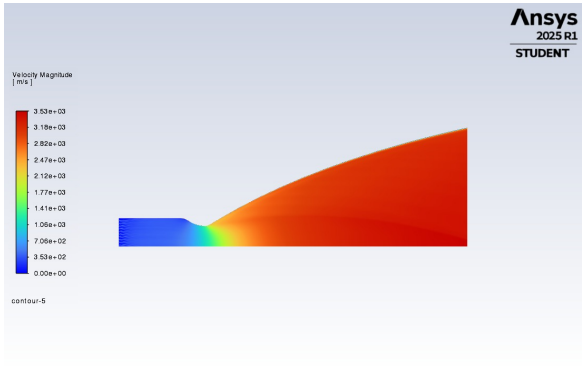


Figure 27: *Velocity Distribution*

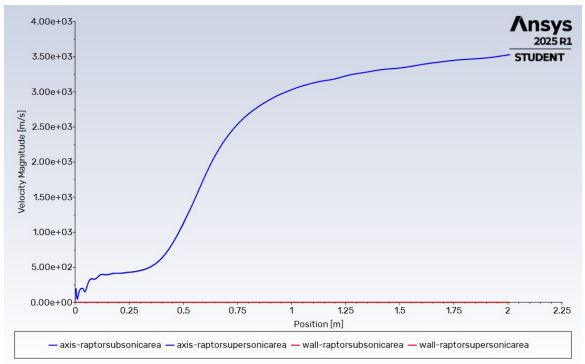


Figure 28: *Velocity in the wall in and in the axis*

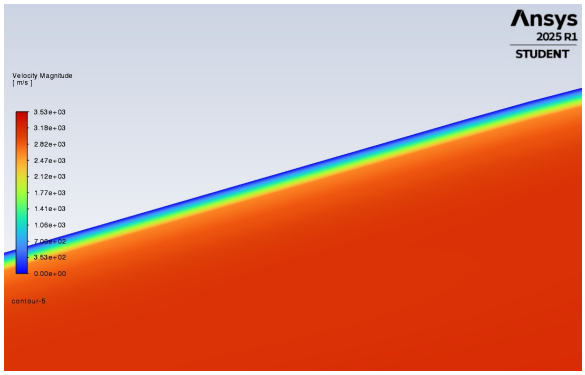


Figure 29: *Velocity Distribution zoom near the wall*

As the combustion products flow through the combustion chamber and into the nozzle, their velocity increases significantly, while both pressure and temperature decrease due to the conversion of thermal and pressure energy into kinetic energy. This acceleration is a result of the nozzle's convergent-divergent geometry, which facilitates supersonic expansion at the exit.

In our simulation, the gas velocity at the nozzle exit reaches approximately $3530\,\mathrm{m\,s^{-1}}$, which indicates a highly efficient acceleration process consistent with expected performance for methane-oxygen propulsion systems. As shown in Figure 29, the velocity profile reveals a sharp drop to $0\,\mathrm{m\,s^{-1}}$ near the nozzle and chamber walls a clear manifestation of viscous effects.

This phenomenon is caused by the no-slip boundary condition, which states that the velocity of a viscous fluid in contact with a solid boundary must match the velocity of the wall (which is zero in this case).

As a result, a velocity gradient is formed between the wall and the free stream, creating a boundary layer where viscous shear stresses are significant. These effects are crucial in rocket engine design, as they impact flow stability, heat transfer, and wall thermal loads.

III.5 Mach Number

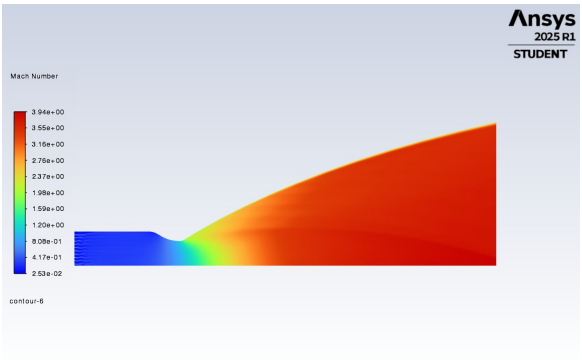


Figure 30: *Mach Number Distribution*

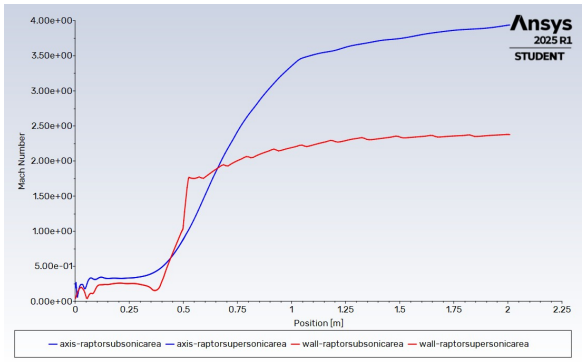


Figure 31: *Mach Number in the wall in and in the axis*

To validate the rocket engine design constructed using the Method of Characteristics (as employed by RPA), the Mach number (Ma) distribution within the engine was analyzed. An optimal design should exhibit a Mach number of 1 at the throat, indicating the transition from subsonic flow in the converging section to supersonic flow in the diverging section of the nozzle. The computed Mach number distribution is presented in Figure 30. At the nozzle exit, a Mach number of approximately 3.94 is observed, which is consistent with expectations.

However, during post-processing, ANSYS displayed unphysically high Mach numbers near the nozzle walls in some cases exceeding Mach 2 despite the local velocity magnitude being effectively zero (e.g., $4.65 \times 10^{-15}\,\mathrm{m\,s^{-1}}$). This discrepancy likely results from numerical artifacts or limitations in ANSYS's built-in Mach number calculation in low-velocity regions.

To address this issue and restore physical accuracy, the Mach number was redefined manually as the ratio of local velocity magnitude to local speed of sound ($M = V/a$). With this corrected definition, the Mach number near the walls correctly approached zero, as expected under the no-slip boundary condition. This refinement was crucial for an accurate interpretation of the flow field and highlights the importance of critically evaluating numerical results. The corrected near-wall Mach distribution is shown in Figure 34.

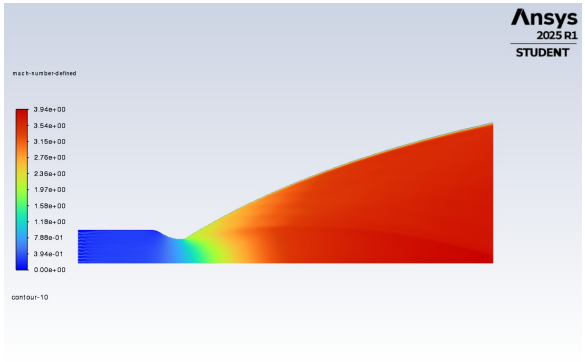


Figure 32: *Corrected Mach Number Distribution*

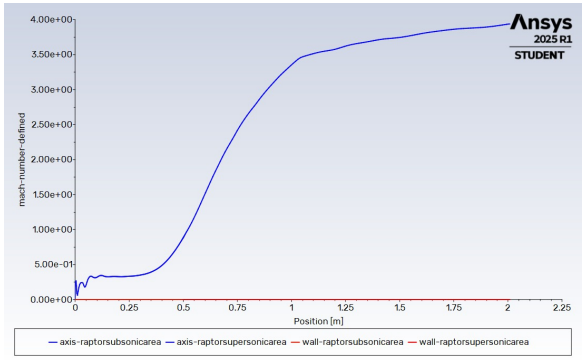


Figure 33: *Corrected Mach Number in the wall in and in the axis*

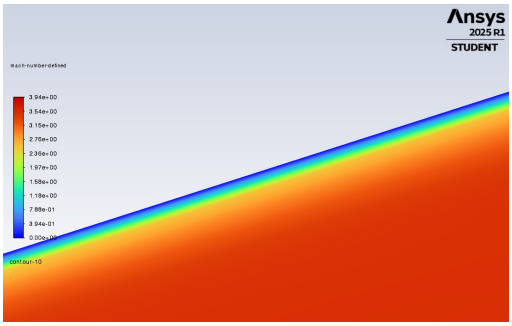


Figure 34: *Corrected Mach Number Distribution zoom near the wall*

III.6 Species Mass Fraction

III.6.1 Reactants Mass Fraction

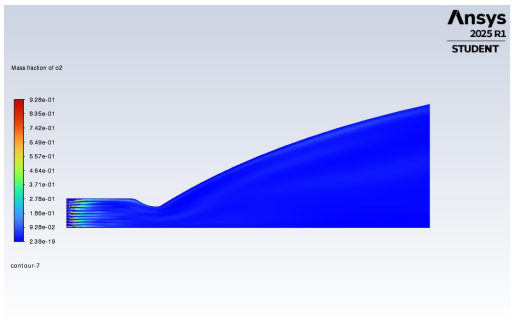


Figure 35: *O_2 Mass fraction*

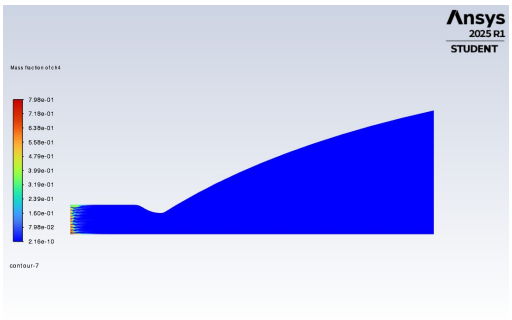


Figure 36: *CH_4 Mass fraction*

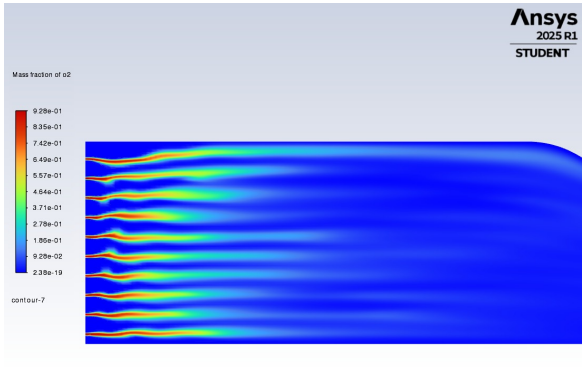


Figure 37: *O_2 Mass fraction zoom in the Combustion Chamber*

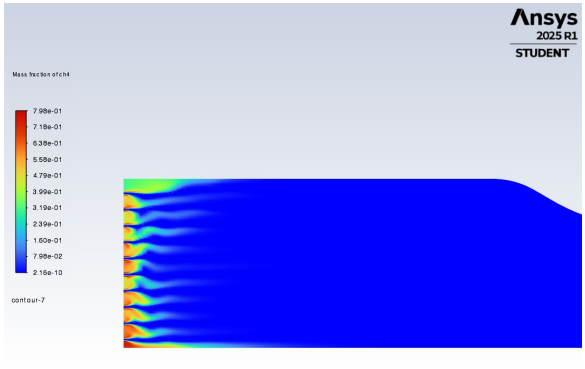


Figure 38: *CH_4 Mass fraction zoom in the Combustion Chamber*

The extremely low mass fractions of CH_4 and O_2 detected downstream of the combustion chamber 2.16×10^{-10} and 2.38×10^{-19} respectively clearly indicate highly efficient combustion. These near-negligible values demonstrate that the fuel and oxidizer have been almost entirely consumed by the end of the combustion process, confirming the effectiveness of the combustion within the chamber.

III.6.2 Products Mass Fraction

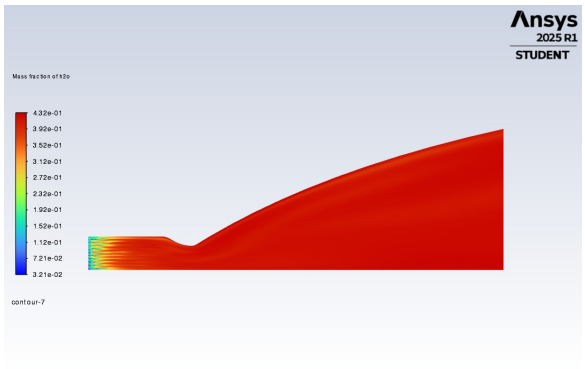


Figure 39: *H_2O Mass fraction*

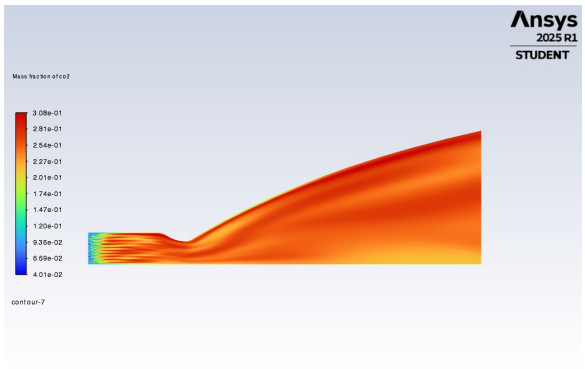


Figure 40: *CO_2 Mass fraction*

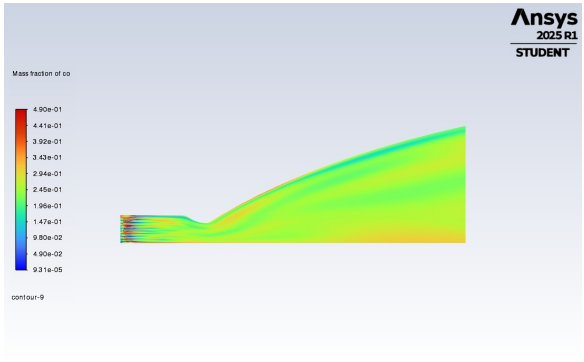


Figure 41: *CO Mass fraction*

The mass fraction of carbon monoxide (CO) exhibits a wide variation, ranging from 9.31×10^{-5} to 4.90×10^{-1}, with an average of 2.45×10^{-1}. This reflects regions of incomplete combustion where CO is present in significant quantities. In comparison, the carbon dioxide (CO_2) mass fraction ranges from 4.01×10^{-2} to 3.08×10^{-1}, with an average of 2.84×10^{-1}.

Interestingly, CO_2 maintains a higher concentration near the wall, despite the temperature in these regions being lower. This may indicate that CO formed in the hotter core regions diffuses toward the wall and gradually oxidizes to CO_2, possibly due to longer residence times or favorable local flow conditions. The observed distribution of CO and CO_2 suggests a spatial progression from incomplete to more complete combustion, with chemical species continuing to evolve even in cooler wall-adjacent zones.

III.6.3 Other Species Mass Fraction

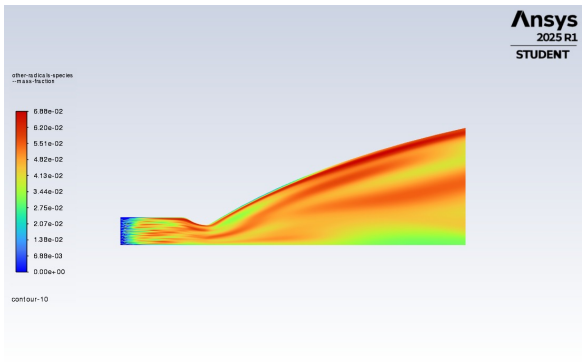


Figure 42: *Other Radicals Species Mass fraction*

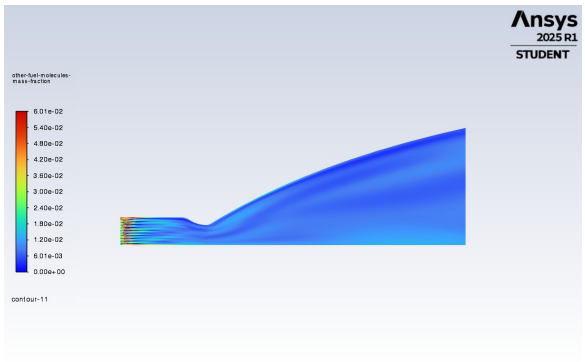


Figure 43: *Other Fuel Molecules Mass fraction*

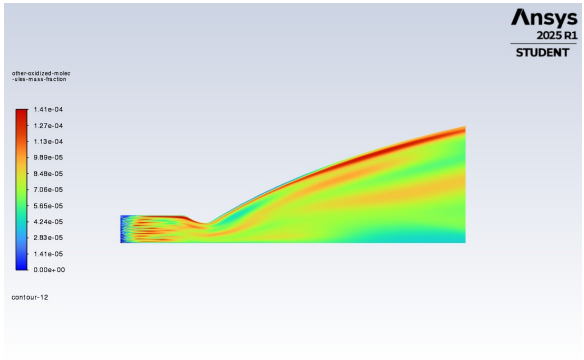


Figure 44: *Other Oxidizer Molecules Mass fraction*

Table 27: *Chemical species groups*

Group	Species
Radicals	H, O, OH, HO_2, CH_3, HCO, CH_2CO
Fuel Molecules	H_2, CH_3OH, C_2H_2, C_2H_4, C_2H_6, C_3H_8
Oxidizer Molecules	H_2O_2, CH_2O

III.7 Results of the 8 Simulations

These results correspond to the first simulation. Using the same methodology, we conducted eight simulations with the boundary conditions defined in table 24. The resulting data is presented in table 28 and will be analyzed in the following section.

Table 28: *Performance Results*

Parameter	Unit	1st	2nd	3rd	4th	5th	6th	7th	8th
Chamber Pressure Pc	bar	305	299	312	291	310	304	311	296
Exit Pressure Pe	Pa	26,000	17,300	26,900	25,100	26,100	19,000	27,000	25,400
Chamber Temperature Tc	K	3,720	3,600	3,880	3,800	3,730	3,580	3,870	3,790
Exit Temperature Te	K	1,680	1,430	1,770	1,760	1,665	1,415	1,755	1,745
Exit Velocity Ve	m/s	3,530	3,350	3,630	3,460	3,500	3,250	3,600	3,420
Exit Mach Number Me	–	3.94	3.76	3.91	3.95	3.92	3.74	3.89	3.93
Thrust T	MN	2.56	2.42	2.64	2.51	2.41	2.22	2.4854	2.3540
Specific Impulse Isp	s	364.90	344.89	375.27	357.59	342.62	315.77	352.98	334.32
Effective Exhaust Velocity C*	m/s	3,578.42	3,382.22	3,680.09	3,506.74	3,359.91	3,096.69	3,461.59	3,278.61

IV Discussion

IV.1 Comparison Between Ansys Results and RPA results

In this comparison, we will use the results from the first and fifth ANSYS simulations and compare them with the results obtained from RPA, as presented in Section II.1.2 (Design Using Rocket Propulsion Analysis (RPA)). The comparison between the ANSYS CFD in Table 29 simulation and RPA (Rocket Propulsion Analysis) results reveals generally good agreement, with most deviations remaining within an acceptable range. The chamber pressure, thrust, specific impulse, and effective exhaust velocity all show discrepancies under 3%, indicating a consistent global performance prediction.

However, notable differences appear in the exit pressure and temperature. The exit pressure in ANSYS is significantly lower (26,100 Pa vs. 86,200 Pa), and the exit temperature is about 15.6% lower. These deviations likely arise due to differences in modeling assumptions: RPA assumes idealized, quasi-one-dimensional flow without accounting for detailed viscous, turbulent, or real-gas effects, whereas ANSYS provides a more comprehensive flow field, including boundary layer and expansion effects.

The lower P_e and T_e in ANSYS are consistent with a more realistic expansion in the nozzle under near-vacuum conditions. Despite these localized differences, the overall thrust and performance metrics remain closely matched, validating the CFD setup and confirming the reliability of both tools within their respective modeling scopes.

Table 29: *Comparison between ANSYS and RPA Results*

Parameter	ANSYS	RPA	Difference (%)
Chamber Pressure Pc (bar)	310	300	-3.23
Exit Pressure Pe (Pa)	26,100	86,200	230.27
Chamber Temperature Tc (K)	3,730	3,791	1.64
Exit Temperature Te (K)	1,665	1,925	15.62
Exit Mach Number Me	3.92	3.86	-1.53
Thrust in Vacuum T (MN)	2.56	2.62	2.34
Thrust at Sea Level T (MN)	2.41	2.45	1.66
Specific Impulse in Vacuum Isp (s)	364	372	2.20
Specific Impulse at Sea Level Isp (s)	342	349	2.05
Effective Exhaust Velocity in Vacuum C* (m/s)	3,578	3,653	2.10
Effective Exhaust Velocity at Sea Level C* (m/s)	3,359	3,425	1.96

IV.2 Why FFSC ?

Table 30: *Simulation Results Comparison WHY FFSC*

Environment	Vacuum			Sea Level		
Simulation	2nd	3rd	4th	6th	7th	8th
O/F	3.60	3.60	3.60	3.60	3.60	3.60
Nature of Chemicals	Pure	Pure	Real Frac.	Pure	Pure	Real Frac.
Fuel Inlet Temp. (K)	180	808	808	180	808	808
Oxidizer Inlet Temp. (K)	90	707	707	90	707	707
Gauge Pressure (atm)	0	0	0	1	1	1
Chamber Pressure Pc (bar)	299	312	290	304	311	290
Exit Pressure Pe (Pa)	17,300	26,900	25,100	19,000	27,000	25,400
Chamber Temp. Tc (K)	3,600	3,870	3,790	3,580	3,870	3,790
Exit Temp. Te (K)	1,430	1,755	1,745	1,415	1,755	1,745
Exit Velocity Ve (m/s)	3,350	3,600	3,420	3,250	3,600	3,420
Exit Mach Number Me	3.76	3.89	3.93	3.74	3.89	3.93
Thrust T (MN)	2.43	2.49	2.35	2.22	2.49	2.35
Specific Impulse Isp (s)	344.89	352.98	334.32	315.77	352.98	334.32
Effective Exhaust Velocity C* (m/s)	3,382.22	3,461.59	3,278.61	3,096.69	3,461.59	3,278.61

The performance comparison between different simulation cases (shown in Table 30 helps clarify why the Full Flow Staged Combustion (FFSC) cycle is employed in engines like the Raptor 2 rather than simpler cycles that inject unreacted propellants directly into the combustion chamber.

In the second and sixth simulations, where pure methane and oxygen are introduced at cryogenic temperatures without preburning, the engine delivers lower performance, evident from lower thrust, specific impulse, and exhaust velocity. In contrast, the third and seventh simulations show improved performance due to elevated inlet temperatures; however, they still assume idealized pure propellants, which is physically unrealistic since such high inlet temperatures cannot be achieved without pre-combustion.

Realistically, high-temperature and real-composition propellants as modeled in the fourth and eighth simulations result from preburning in the FFSC cycle, where both fuel and oxidizer streams are partially combusted in separate preburners before entering the main chamber. This not only raises the inlet temperature but also ensures a more uniform and efficient combustion process.

Furthermore, the FFSC cycle offers:

- Better turbine efficiency due to lower pressure drops across the system
- Improved cooling of critical engine components by routing propellants through them prior to combustion
- Higher performance combustion characteristics
- Enhanced thermal management capabilities

The Full-Flow Staged Combustion (FFSC) cycle represents a major advancement over conventional propulsion cycles such as the Gas Generator (GG) and traditional Staged Combustion (SC) systems. Unlike these earlier designs, FFSC utilizes dual preburners one fuel-rich and one oxidizer-rich allowing complete gasification of all propellants before injection into the main combustion chamber. This architecture eliminates the need for inter-propellant seals and reduces turbine complexity, enabling a higher total mass flow through the turbines at significantly lower temperatures. As a result, FFSC engines exhibit improved durability, enhanced reusability, and greater thermal resilience critical features for long-term, multi-flight missions such as SpaceX's Starship program.

Furthermore, by ensuring that both propellant streams are preheated via regenerative cooling channels prior to combustion, FFSC not only improves combustion efficiency and chamber wall cooling but also contributes to structural longevity. CFD results from this study confirmed these advantages, demonstrating near-complete propellant consumption (CH_4 and O_2 residuals $< 10^{-10}$), high combustion temperatures, and excellent agreement with real Raptor 2 engine performance achieving a specific impulse exceeding 330 s and thrust deviations below 3 %.

Compared to GG cycles, which discard unburned propellant and suffer from lower I_{sp}, and SC cycles, which preburn only one stream and may lead to combustion non-uniformities, the FFSC cycle offers superior performance, reliability, and thermal management, making it the most advanced and practical choice for next-generation reusable launch systems.

Altogether, these factors make FFSC engines capable of achieving higher performance, better reusability, and enhanced thermal management compared to simpler combustion cycles.

IV.3 The Reasons Behind O/F=3.6

Table 31: *Performance Comparison by O/F Ratio*

Parameter	O/F = 3		O/F = 3.6	
Environment	Vacuum	Sea Level	Vacuum	Sea Level
Chamber Pressure Pc (bar)	305	291	310	296
Exit Pressure Pe (Pa)	26,000	25,100	26,100	25,400
Chamber Temperature Tc (K)	3,720	3,800	3,730	3,790
Exit Temperature Te (K)	1,680	1,760	1,665	1,745
Exit Velocity Ve (m/s)	3,530	3,460	3,500	3,420
Exit Mach Number Me	3.94	3.95	3.92	3.93
Thrust T (MN)	2.57	2.52	2.41	2.35
Specific Impulse Isp (s)	364.90	357.59	342.62	334.32
Effective Exhaust Velocity C* (m/s)	3,578.42	3,506.74	3,359.91	3,278.61

At first glance, the simulation results in Table 31 clearly indicate that an oxidizer-to-fuel ratio (O/F) of 3 yields superior performance compared to an O/F of 3.6. Specifically, the O/F=3 case demonstrates:

- 6.63% higher vacuum thrust (2.57 MN vs. 2.41 MN)
- 6.11% higher specific impulse in vacuum (364.9 s vs. 342.6 s)
- Reduced thermal loads (3,720 K vs. 3,730 K chamber temperature)

This suggests that an O/F of 3 is thermodynamically more efficient for the main combustion chamber. However, SpaceX's operational Raptor engines use an O/F of 3.6, which appears contradictory. The key explanation lies in preburner performance:

- Current simulations for O/F=3 used identical preburner outlet compositions as the O/F=3.6 case (from Table 2)
- This assumption is physically unrealistic - preburner output mass fractions should vary with O/F ratio
- At O/F=3, fuel-rich preburner operation would produce different equilibrium species

To resolve this discrepancy, we will:

1. Recompute preburner equilibrium compositions for O/F=3 using Cantera
2. Rerun simulations with corrected inlet conditions
3. Document the complete methodology for deriving preburner outputs

This approach will ensure physically consistent modeling of the full-flow staged combustion cycle across different O/F ratios.

In our simulation program, the user import a yaml mechanism file of the combustion species and reactions and also contain therodynamics data and also the user inputs key parameters related to the preburner: the mass flow rate, the internal pressure of the preburner, the inlet temperatures of both fuel and oxidizer, the desired target exit temperature, the acceptable temperature tolerance, and the preburner type (fuel-rich or oxidizer-rich). Additionally, the user provides the species fractions of the propellants. The program then performs multiple simulations with varying mixture ratios (O/F) in the preburner, aiming to identify the exact OF that results in an exit temperature within the specified tolerance. Once the optimal O/F is found, the program conducts a detailed simulation at that mixture ratio to determine the mass and mole fractions of the combustion products at the outlet of the preburner. This allows for a more accurate characterization of the preburner output, which can be used for further engine performance analysis.

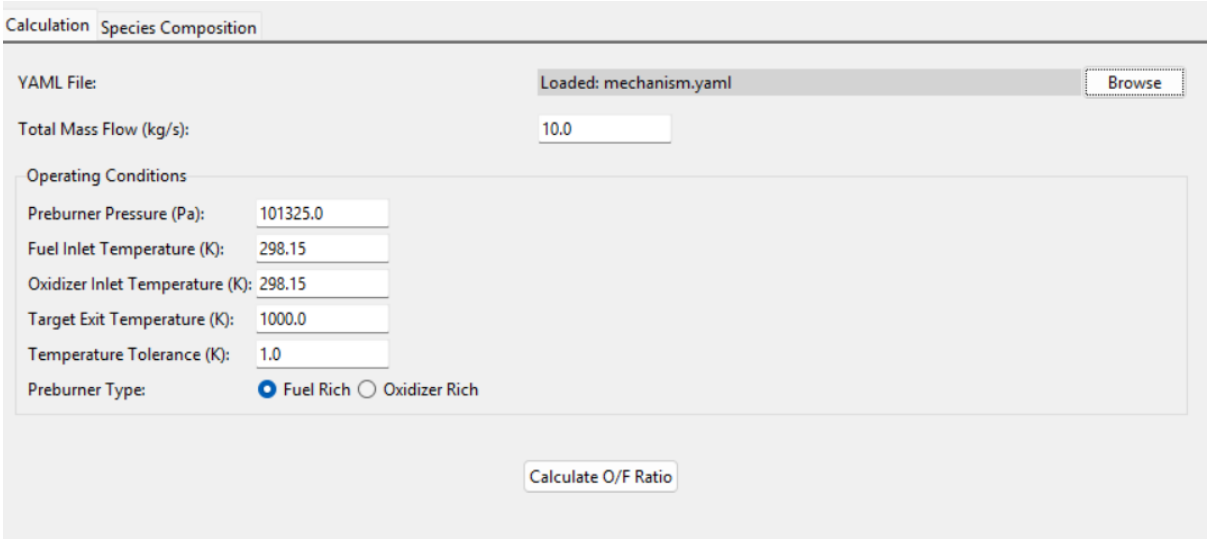


Figure 45: *Program interface*

Table 32: *Results of O/F Cantera Simulation*

Parameter	O/F = 3		O/F = 3.6	
Preburner	Fuel Rich	Oxidizer Rich	Fuel Rich	Oxidizer Rich
CH_4 Mass Flow (kg/s)	165.65	12.75	143.44	13.32
O_2 Mass Flow (kg/s)	13.34	526.24	11.55	549.67
O/F of preburner	0.0805	41.24	0.0805	41.24
Total Mass Flow (kg/s)	179	539	155	563
CH_4 Total Mass Flow (kg/s)	178.40		156.76	
O_2 Total Mass Flow (kg/s)	539.58		561.22	

Table 33: *Composition of combustion products at preburner outlets from Cantera O/F=3 (mass fractions)*

Species	Fuel (CH_4 preburner outlet)	Oxidizer (LOX preburner outlet)
CH_4 (Methane)	0.82	0
O_2 (Oxygen)	0	0.94
CO_2 (Carbon dioxide)	0.1	0.032
H_2O (Water vapor)	0.071	0.026
CO (Carbon monoxide)	0.0035	0
H_2 (Hydrogen)	0.0017	0
C_2H_6 (Ethane)	0.0019	0

As shown in Table 32, both configurations O/F = 3 and O/F = 3.6 use the same oxidizer-to-fuel ratio in the preburners; however, the total mass flow and the individual species mass flows within each preburner differ significantly. Notably, the O/F = 3 configuration requires more methane and less oxygen compared to the O/F = 3.6 case. Furthermore, Table 33 demonstrates that the outlet mass fractions of the species are identical in both cases, which validates the accuracy of the simulation and confirms that the preburners are not the determining factor behind the selection of O/F = 3.6 over O/F = 3. This strongly suggests that other considerations influence the choice of mixture ratio.

Although O/F = 3 typically offers better performance, SpaceX opts for O/F = 3.6 in the Raptor engine, primarily due to system-level optimizations. One critical factor is propellant storage. A lower O/F ratio implies a higher methane demand, which necessitates larger methane tanks. Given that liquid methane has a relatively low density ($\sim$422 kg/m^3) compared to liquid oxygen ($\sim$1141 kg/m^3), accommodating this additional volume significantly increases tank size and structural mass. Moreover, larger methane tanks require more insulation to maintain cryogenic conditions, as well as more complex pressurization and management systems. These additions not only increase the dry mass of the vehicle but also occupy more internal space, which can negatively affect payload capacity and structural layout. In contrast, a higher O/F ratio like 3.6 allows for smaller, lighter methane tanks, resulting in a more compact, mass-efficient, and structurally optimized design. While O/F = 3 might provide slightly higher thrust per kilogram of propellant, the increased complexity and mass penalties of storing more methane make it less favorable. Therefore, O/F = 3.6 represents a well-balanced trade-off between engine performance, vehicle mass distribution, reusability, and overall mission feasibility.

IV.4 Comparison Between Vacuum and Sea Level

Table 34: *Performance Comparison: Vacuum vs Sea Level*

Parameter	Vacuum	Sea Level	Difference	% Difference
Chamber Pressure Pc (bar)	291.00	296.00	-5.00	-1.72
Exit Pressure Pe (Pa)	25,100.00	25,400.00	-300.00	-1.20
Chamber Temperature Tc (K)	3,800.00	3,790.00	10.00	0.26
Exit Temperature Te (K)	1,760.00	1,745.00	15.00	0.85
Exit Velocity Ve (m/s)	3,460.00	3,420.00	40.00	1.16
Exit Mach Number Me	3.95	3.93	0.02	0.51
Thrust T (MN)	2.52	2.35	0.16	6.51
Specific Impulse Isp (s)	357.59	334.32	23.26	6.51
Effective Exhaust Velocity C* (m/s)	3,506.74	3,278.61	228.13	6.51

The comparison between vacuum and sea-level simulation results reveals several insightful physical phenomena tied to the operating conditions of a rocket engine and atmospheric effects. Firstly, we observe a slightly higher chamber pressure at sea level (296 bar) compared to vacuum conditions (291 bar), with a minor decrease of about 1.7%. This may seem counterintuitive at first, but it can arise from adjustments in nozzle back pressure and flow dynamics within the combustion chamber due to external pressure forces. Despite the chamber being highly pressurized,

slight feedback from the ambient conditions can subtly influence internal pressure equilibrium.

The exit pressure is also slightly higher at sea level (25,400 Pa vs. 25,100 Pa), which is expected since the nozzle exhausts into a denser atmosphere. In a vacuum, there's no external resistance to flow expansion, so the gases expand more fully, resulting in a lower exit pressure. The chamber temperature shows a negligible increase (10 K higher in vacuum), which may be attributed to slight variations in combustion efficiency or heat loss behavior under different boundary conditions, though it's within normal tolerance.

More interestingly, the exit temperature is higher in vacuum (1,760 K vs. 1,745 K), which aligns with the expectation that in the absence of atmospheric pressure, the gas can expand more freely and maintain more of its internal energy as thermal content before full kinetic conversion. However, the exit velocity is significantly higher in vacuum by 40 m/s, indicating that more of the combustion energy is effectively converted into kinetic energy due to the lack of back pressure. This results in a higher exit Mach number as well (3.95 vs. 3.93), though the change is small.

The most striking differences come in thrust, specific impulse, and characteristic exhaust velocity (C^*). The vacuum case delivers a thrust of 2.517 MN compared to 2.354 MN at sea level a gain of over 6.5%, which directly translates to a proportional increase in specific impulse (357.6 s vs. 334.3 s). This is because in vacuum, the exhaust expands more fully and exits the nozzle at a higher velocity, creating a larger momentum change. Since I_{sp} is directly proportional to exhaust velocity, this is a key driver in the observed performance boost. Similarly, the C^* value, a measure of the combustion chamber efficiency independent of the nozzle, is also higher in vacuum (3,506 m/s vs. 3,278 m/s), showing that the effective energy release and acceleration of gases is more optimal in space.

Overall, these differences underscore fundamental principles of rocket physics: ambient pressure strongly influences nozzle expansion, which in turn affects exhaust velocity and thrust. In vacuum, rockets operate more efficiently due to the ability to fully expand exhaust gases without atmospheric resistance. This explains why vacuum-specific performance metrics are always higher and why nozzle design often involves trade-offs to optimize expansion across both sea-level and vacuum phases of flight.

IV.5 Comparison Between our Results and Real Raptor 2 engine

Table 35: *Comparison between Raptor 2 and Our Simulation*

Parameter	Raptor 2	Our Raptor 2	Difference	% Difference
Chamber Pressure Pc (bar)	300.00	296.00	4.00	1.33
Thrust T (MN) (Sea Level)	2.30	2.35	-0.05	-2.17
Specific Impulse Isp (s) (Sea Level)	327.00	334.00	-7.00	-2.14
Effective Exhaust Velocity C* (m/s) (Sea Level)	3,206.77	3,275.42	-68.65	-2.14

When comparing the results of our simulation to the real Raptor 2 engine developed by SpaceX, we observe slight differences that may initially suggest improved performance in our model. For instance, our simulated sea-level thrust reached 2.35 MN compared to Raptor 2's 2.3 MN, and our specific impulse (I_{sp}) at sea level was 334 s versus 327 s for the real engine. Similarly, our effective exhaust velocity (C^*) was 3275 $\mathrm{m\,s^{-1}}$, which is slightly higher than the actual value of approximately 3207 $\mathrm{m\,s^{-1}}$. At first glance, these results may appear to indicate superior performance; however, this interpretation must be approached with caution and placed in the proper context of real-world rocket engine design and operation.

One crucial factor to consider is that our simulation did not account for the complex regenerative cooling system used in the real Raptor 2. In an actual engine:

- A portion of the propellants (especially cryogenic liquid methane) is diverted through cooling channels
- This reduces the total mass flow available for combustion
- The thermodynamic state (temperature, pressure) of the propellants is affected
- Overall performance metrics (thrust, I_{sp}) are slightly decreased

In contrast, our simulation assumes idealized adiabatic conditions without:

- Heat losses to engine components
- Material limitations
- Cooling mass flow requirements

Moreover, our model does not include other practical engineering considerations:

- Material strength limits and manufacturing constraints
- Injector non-uniformity and combustion instability
- Turbopump efficiency losses
- Boundary layer effects and turbulence

SpaceX optimizes the Raptor 2 for:

- Reliability over multiple flights
- Thermal management and durability
- Practical manufacturability
- Safety margins

In conclusion, while our simulation yielded promising results with slightly improved figures over the actual Raptor 2, this does not imply that our design surpasses SpaceX's engineering. Rather, it underscores the importance of:

- Incorporating thermal and structural complexities
- Modeling fluid-dynamic losses
- Accounting for real-world engineering constraints

True engine performance is not defined by theoretical efficiency alone, but by the robust integration of:

- Performance metrics
- Operational stability
- Long-term durability
- Flight-proven safety

domains in which SpaceX has invested years of development and testing.

V Conclusion

This project successfully performed a high-fidelity Computational Fluid Dynamics (CFD) simulation of the internal flow dynamics in the combustion chamber and nozzle of SpaceX's Raptor 2 engine. Leveraging a hybrid methodology incorporating **NASA CEA**, **Rocket Propulsion Analysis (RPA)**, and **Cantera**, the study validated key thermodynamic, geometric, and performance parameters, yielding results closely aligned with empirical data. The simulation achieved a **thrust of** 2.35 MN and a **specific impulse of** 334 s **at sea level**, with errors remaining below **3%**, thus affirming the accuracy and robustness of the modeling approach.

The study also confirmed the high combustion efficiency of the **methane–oxygen propellant pair**, demonstrating near-complete reactant consumption and optimal exhaust expansion. Detailed species mass fraction analysis revealed proper combustion behavior, with minimal unburnt CH_4 and O_2 at the nozzle exit. The analysis highlighted the benefits of the **Full-Flow Staged Combustion (FFSC)** cycle, particularly in terms of combustion completeness, and improved overall engine durability. Furthermore, the rationale behind SpaceX's choice of an **O/F ratio of 3.6** was explored as a design trade-off between performance, cooling efficiency, and propellant tank volume optimization.

Key Findings:

- Validated major performance parameters (thrust, I_{sp}, P_c) with <3% deviation from real Raptor 2 data.
- Demonstrated FFSC advantages in efficiency, thermal management, and reusability.
- Justified the use of O/F = 3.6 for system-level optimization.
- Compared performance under sea-level and vacuum conditions, confirming superior vacuum expansion efficiency.

Future Work: While the current model incorporates detailed chemistry and advanced turbulence treatment, several assumptions such as **adiabatic walls** and **steady-state flow** introduce limitations. Future studies should aim to:

- **Integrate regenerative cooling systems** to evaluate thermal loading and chamber wall temperatures.
- **Conduct transient analyses** to capture ignition dynamics, startup/shutdown sequences, and combustion instability.
- **Implement 3D and multiphase flow models** to better represent injector spray dynamics and radial flow features.
- **Refine turbulence modeling** through Large Eddy Simulation (LES) to improve resolution of vortical structures.

Broader Impact: This research contributes to the growing body of knowledge required to design **high-performance reusable rocket engines**, with direct relevance to **SpaceX's interplanetary transportation goals**, including the colonization of Mars. It also reinforces the importance of **CFD as a critical tool** in modern propulsion design, enabling cost-effective, accurate performance prediction ahead of experimental validation.

Ultimately, this project lays a strong foundation for future high-fidelity modeling of staged combustion engines and supports the evolution of **next-generation aerospace propulsion systems**..

References

1. S. Gordon and B. J. McBride, *Computer Program for Calculation of Complex Chemical Equilibrium Compositions and Applications (NASA RP-1311)*, NASA, 1996.
2. NASA, "Chemical Equilibrium with Applications (CEA)," [Online]. Available: https://www.grc.nasa.gov/www/CEAWeb/.
3. NASA Glenn Research Center, *Chemical Equilibrium with Applications (CEA)* [Software], NASA, 2024. [Online]. Available: https://www.nasa.gov/cea
4. A. Ponomarenko, *RPA: Design Tool for Liquid Rocket Engine Analysis*, 2009.
5. Rocket Propulsion Analysis, "Rocket Propulsion Analysis," [Online]. Available: https://www.rocket-propulsion.com/.
6. RP Software + Engineering UG, *Rocket Propulsion Analysis (RPA)* [Software]. [Online]. Available: https://www.rocket-propulsion.com
7. SpaceX, "Raptor Engine," [Online]. Available: https://www.spacex.com/vehicles/raptor/.
8. Wikipedia contributors, "SpaceX Raptor," Wikipedia, Jun. 28, 2024. [Online]. Available: https://en.wikipedia.org/wiki/SpaceX_Raptor
9. Everyday Astronaut, "Raptor 1 vs Raptor 2: What did SpaceX change?," Jul. 14, 2022. [Online]. Available: https://everydayastronaut.com/raptor-1-vs-raptor-2-what-did-spacex-change/
10. Wikipedia contributors, "Staged combustion cycle," Wikipedia, Apr. 15, 2024. [Online]. Available: https://en.wikipedia.org/wiki/Staged_combustion_cycle
11. Wikipedia contributors, "Full-flow staged combustion cycle," Wikipedia, [Online]. Available: https://en.wikipedia.org/wiki/Full-flow_staged_combustion_cycle.
12. Wikipedia contributors, "RD-270," Wikipedia, May 3, 2024. [Online]. Available: https://en.wikipedia.org/wiki/RD-270
13. Wikipedia contributors, "RD-270," Wikipedia, [Online]. Available: https://en.wikipedia.org/wiki/RD-270.

14. Aerojet Rocketdyne, “Integrated Powerhead Demonstration,” [Online]. Available: https://www.rocket.com.

15. J. M. Jones, W. F. Sack, W. D. Boyce, and W. A. Hayes, “Integrated Powerhead Demonstration: Full Flow Cycle Development,” in *Proc. 35th AIAA/ASME/SAE/ASEE Joint Propulsion Conf.*, 1999. [Online]. Available: https://doi.org/10.2514/6.1999-2483

16. Wikipedia contributors, “Integrated Powerhead Demonstrator,” Wikipedia, Nov. 12, 2023. [Online]. Available: https://en.wikipedia.org/wiki/Integrated_Powerhead_Demonstrator

17. Wikipedia contributors, “Integrated Powerhead Demonstrator,” Wikipedia, [Online]. Available: https://en.wikipedia.org/wiki/Integrated_Powerhead_Demonstrator.

18. Stoke Space, “Stoke Space Completes First Successful Hotfire Test of Full-Flow, Staged-Combustion Engine,” Jun. 11, 2024. [Online]. Available: https://www.stokespace.com/

19. GeekWire, “Stoke Space successfully test-fires engine for reusable Nova rocket,” Jun. 11, 2024. [Online]. Available: https://www.geekwire.com/2024/stoke-space-successfully-test-fires-engine-for-reusable-nova-rocket/

20. Aviation Week Network, “Stoke Space Begins Testing Full-Flow Staged Combustion Engine,” *Aviation Week*, Feb. 6, 2024. [Online]. Available: https://aviationweek.com/defense-space/space/stoke-space-begins-testing-full-flow-staged-combustion-engine

21. Everyday Astronaut, “Starhopper’s Untethered Hop Marks First Use of Full-Flow Staged Combustion Engine in Flight,” Jul. 26, 2019. [Online]. Available: https://everydayastronaut.com/starhopper-hop-raptor-first-flight/

22. Cantera, “Open-source chemical kinetics, thermodynamics, and transport,” [Online]. Available: https://cantera.org/.

23. D. G. Goodwin, R. L. Speth, H. K. Moffat, and B. W. Weber, *Cantera: An Object-Oriented Software Toolkit for Chemical Kinetics, Thermodynamics, and Transport Processes (Version 3.0)* [Open source software], 2023. [Online]. Available: https://cantera.org

24. GRI-Mech, “GRI-Mech 3.0,” University of California, Berkeley. [Online]. Available: http://combustion.berkeley.edu/gri-mech/.

25. G. P. Smith et al., "GRI-Mech 3.0: A detailed chemical kinetic mechanism for the combustion of hydrocarbon fuels," 1999. [Online]. Available: http://www.me.berkeley.edu/gri_mech

26. R. W. Claus, B. J. McBride, and R. Foster, "Application of a Chemical Equilibrium Analysis to In-Situ Lunar Resource Utilization," in *Proc. 41st AIAA/ASME/SAE/ASEE Joint Propulsion Conf.*, 2005. [Online]. Available: https://doi.org/10.2514/6.2005-4432

27. S. Gordon and B. J. McBride, *Computer Program for Calculation of Complex Chemical Equilibrium Compositions and Applications. Part 1: Analysis (NASA RP-1311)*, NASA Lewis Research Center, 1994. [Online]. Available: https://ntrs.nasa.gov/citations/19940013151

28. C. Latimier, "Numerical analysis of Raptor engine's combustion chamber," Concordia University; Polytechnique Montréal, 2024. HAL Id: hal-04536141. [Online]. Available: https://hal.science/hal-04536141v1

29. M. Piunti, F. Persico, A. Shytani, and S. Pasetti, "Preliminary design of a Raptor-like engine," Politecnico di Milano, Jul. 2022. DOI: 10.13149/08.12.136351.1770. [Online]. Available: https://www.researchgate.net/publication/363367182